Optimization of MAPbI$_3$ perovskite film

prepared via meniscus-guided blade coating

by

Xingquan Chen

Submitted in partial fulfillment of the requirements

for the degree of Master of Science

at

Dalhousie University

Halifax, Nova Scotia

December 2022

Dalhousie University is located in Mi'kma'ki, the

ancestral and unceded territory of the Mi'kmaq.

We are all Treaty people.

DEDICATION PAGE

Thanks to my mom Hongbo Sun, and my father Guoyu Chen.

Thanks to Dr. Ghada Koleilat and Dr. Micheal Cada for supporting my master's program financially.

Thanks to Dr. Hinds for the outline organization.

Thanks to my girlfriend Ying Zhou for supporting me.

Thanks to my partner Ph.D. student Ghada Abdelmageed the experimental support.

Contents

List of tables

List of Figures

List of abbreviations used

MAI	methylammonium iodide
PSC	perovskite solar cells
PCE	power conversion efficiency
FF	fill factor
J_{sc}	short current density
V_{oc}	open circuit voltage
DMF	dimethylformamide
DMSO	dimethyl sulfoxide
MACl	methylammonium chloride
GBL	γ-butyrolactone
DMA	N, N-dimethylacetamide
ETL	electron transport layer
HTL	hole transport layer
PV	photovoltaic
CPC	compound parabolic concentrator
DPT	double parabolic trough concentrator
SEM	scanning electronic microscope
UV-Vis	Ultraviolet-Visible
CLSM	confocal laser scanning microscopy
PL	Photoluminescence
XRD	X-ray diffraction
FTIR	Fourier transform infrared
Z	impedance
C	capacitance
R	resistance
L	inductance

Abstract

In this study, perovskite layers were prepared by using a one-step blade coating process with different binary solvent and methylammonium (MA) cation concentrations. The optoelectronic properties of $CH_3NH_3PbI_3$ (MAPbI$_3$) perovskite films were determined. The mixed solvent solution produces a uniform perovskite layer with a larger grain size than a single solvent. In addition, the excess MA cation reduces the active layer defect density, impedance, and improves the absorptions that the solar cell performance positively affects. This was confirmed during the simulation process by SCAPS. Furthermore, we investigated the non-tracking light concentrator, which can be used in a solar cell system to increase the efficiency of solar cells.

CHAPTER 1   **Introduction**

Solar power is one of the promising power sources to reduce carbon emissions. Crystalline silicon has been the go-to choice in recent years because it is more efficient and affordable than a traditional silicon-based solar panel. Other materials only cover 5% of the market. However, silicon is not ideal for transportation due to its fragility and rigidity. Further, its efficiency has almost reached the theoretical limit. In addition, the manufacture of silicon solar panels is a dirty business due to the intense heat needed to remove impurities from silicon. Thus, researchers and companies have been looking for alternatives.

The manufacture of perovskite solar cells (PSC) is promising as it provides high efficiency combined with a simple manufacturing process that does not require heat. Also, perovskite solar cells can be manufactured with much thinner layers. Perovskite is a type of semiconductor material that has a simple cubic symmetry such as calcium titanium oxide ($CaTiO_3$). This type of semiconductor has been used in fuel cells, glass-ceramics, superconducting devices, and more, but it was only applied to solar cells in 1999. The solar cell efficiency has increased from 3.8% in 2009 to 25.7% in 2021 and 29% today in single-junction architectures (Kita et al. 2018). Perovskites are easy to synthesize and are considered the future of solar cells because their distinctive structures have shown great potential for high performance and low production costs. In laboratories, perovskite cells are manufactured by spin-coating, spray-coating, or blade-coating onto a substrate, which is a material that provides a surface for chemicals to crystallize on.

In addition, the power conversion efficiency (PCE) of solar cell devices can be enhanced by

adding a light concentrator to accumulate sunlight onto the solar cell device surface. In this work, a concentrator was designed that can concentrate efficiently from wide acceptance angles without the need of a tracker.

Furthermore, we optimized the perovskite film with exceeded methylammonium iodide (MAI), mixed different ratios of poly solvent — dimethylformamide (DMF) and dimethyl sulfoxide (DMSO), and used methylammonium chloride (MACl) in MAPbI$_3$ to control nucleation and crystal growth, which affected surface morphology, grain size, defect passivation and crystal phase purity, by the one-step blade-coating method.

Therefore, the purpose of this study is:

1. Investigated the perovskite samples electronic property use different technique.

2. Simulated perovskite solar cell devices by SCAPS (determine the effective of device thickness, layer defect density and interface defect density).

3.   Simulated reflector type concentrator by COMSOL-Multiphysics and determine different types of concentrator concentration efficiency.

CHAPTER 2   Literature Review

2.1 Perovskite material

To understand perovskite solar cells, we must first introduce what they are. Perovskites are a large family of compounds that have the chemical structure shown in Figure 1, where the A ion (grey spheres) is a relatively large cation at the center of the unit cell, and the B ion (blue spheres) is a smaller cation at the corners. The three X anions (red spheres) are at the centers of the edges of the unit cell (Johnsson and Peter. 2008).
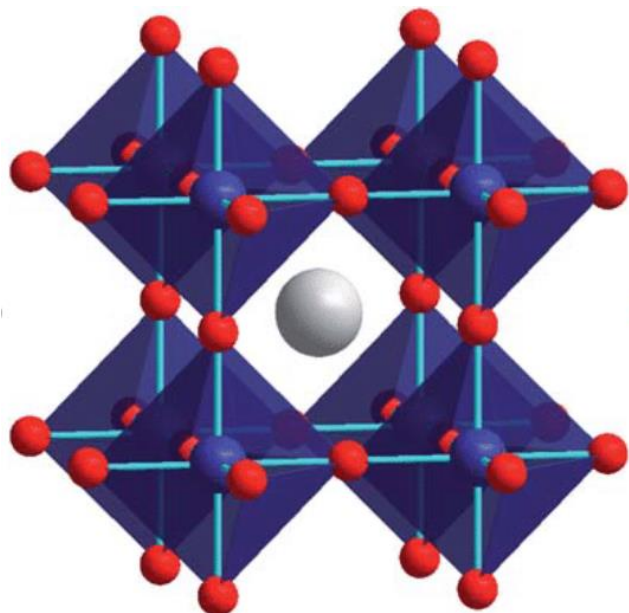
Figure 1. The cubic ABX3 perovskite structure (Johnsson and Peter. 2008)

2.2 Coating technique

To develop perovskite solar cells, the challenge is scalability. Spin-coating is currently the first

choice to obtain a smooth and thin film. However, it is only available in lab-scale production

because of technique restrictions and the fact that 90% of the initial solution is wasted (Marques

et al. 2021). To be compatible with industrial scale, the blade-coating method, as shown in

Figure 2, is an industry-friendly technique that can be commercialized. Blade coating is used to

form films which cover a large area, are free of pinholes, and have a well-defined thickness. The

technique works by placing a sharp blade at the fixed distance from the surface that needs to be

covered. The coating solution is then placed in front of the blade and the blade is moved across

in line with the surface, creating a wet film. Then, the film is moved to a hotplate to dry. The

aim of using the annealing process is to evaporate solvent for perovskite deposition (Jung et al.

2019). Recent experiments show that blade coating at 50 °C results in a large needle-like

morphology with roughness and non-uniformity. It cannot be used in solar cell devices. Coating

at a higher temperature (150 °C) results in fewer nuclei and more growth. Hence, large grains

with full coverage of the film was obtained (Zhong et al. 2018). The blade coating is suitable for

depositing a uniform layer over a large area with a high blade moving speed

(0.1mm/s~0.5mm/s). The quality of film also depends on the blade angle, the relative gap

between substrate and blade, and the substrate temperature (Minsu et al. 2019).
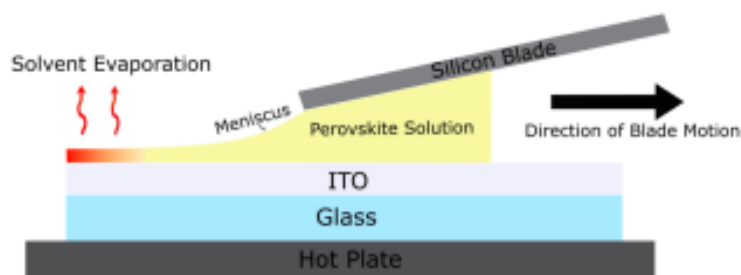
Figure 2. Illustration of blade-coating deposition technique

2.3 Solvent study

The physicists William Shockley and Hans-Joachim Queisser calculated the theoretical maximum efficiency of the silicon single junction solar cell at 33% with a bandgap of 1.34 eV. This is known as the Shockley-Queisser limit (Kita et al. 2019). The perovskite material is a type of semiconductor material with the best performing solar cells bandgap from 1.48 eV to 1.62 eV and it can be tuned to absorb different colors in the solar spectrum. This bandgap flexibility opens another application for these solar cells in high-performance tandem device configurations that achieve efficiency above 30%, such as the multi-junction solar cell (Rohit et al. 2017).

Bandgap tuning is accomplished by changing the morphology of perovskite materials. Mbilo et al. 2019 shows the crystal morphology significantly affects the bandgap. The composition and concentration of chemicals and different mole ratio of solvent affect the crystal morphology, which includes uniform and dense surface morphology, large grain size, perovskite crystal phase purity and crystallinity (Jung et al. 2019). Thus, the solution chemistry, particularly the solvent engineering technique, plays an important role in controlling nucleation and crystal growth to achieve a uniform and pinhole free perovskite layer with full surface coverage. A poly solvent involves dimethylformamide (DMF), γ-butyrolactone (GBL), dimethyl sulfoxide (DMSO) and N, N-dimethylacetamide (DMA), which can be used in a precursor solution, and spin coating or blade coating can be used to coat on the substrate. Then films removed by annealing on a hot plate, causing the perovskite crystal growth to obtain a perovskite film. Perovskite films use neat DMF and show a fiber-like surface morphology with lots of pinholes, which are bad for photovoltaic performance. In addition, using pure DMF as a precursor solution makes it hard to control crystal growth and nucleation, which causes the surface to be rough and full of pinholes.

(Jung et al. 2019). To improve the performance of the perovskite layer, another poly solvent, dimethyl sulfoxide (DMSO), is used, which can retard the reaction between methylammonium iodide (MAI) and lead halide (PbI_2). That leads to MAI-DMSO-PbI_2 converting to crystalline perovskite structures. In addition, due to the low solubility of a single solvent, the formation of perovskite film is hindered, and the efficiency of PSC is lowered. Thus, many studies investigated the co-solvent or binary solvent to improve the active layer surface roughness, crystal size, and smoothness (Liu & Ke. 2020). The spin-coated film was optimized by adding 20% to 40% of DMF into DMSO to obtain a high quality, uniform surface, and increase film thickness (Cai et al. 2015).

2.4 Deposition method

In general, a perovskite layer has two fabrication methods, one is called one-step deposition and the other is two-step deposition (Tian et al. 2019). Two-step deposition involves, first, depositing a layer of inorganic material (such as PbI_2 in this study) by spin coating or blade coating, and then depositing metal halide (Burschka et al. 2013). Taking the fabrication of $MAPbI_3$ as an example, the substrate is first dipping PbI_2 and then dipping MAI to form perovskite. However, the two-step method has weak chemical bonding as well as weak van der Waals interactions on PbI_2, which allows an easy insertion of other molecules between I-Pb-I planes (Burschka et al., 2013). This can be caused by the incomplete transformation from PbI_2 into high quality perovskite film (Chen et al. 2017). One-step deposition is much easier and more convenient to fabricate high quality and uniform perovskite films, if the reactants are mixed well (Tian et al. 2019). What is more, using one-step deposition enhances the reaction kinetics, and transforming PbI_2 to $MAPbI_3$ can be completed in a short time (Burschka et al.,

2013).

2.5 Role of MAI and MACl

To overcome the technical obstacle to the one-step solution deposition method for high-quality perovskite film, solution additives (such as Cl compound and MA additive) have been shown to be effective agents on perovskite thin films (Diau et al. 2018). A Cl compound, such as CH_3NH_3Cl or MACl, can control the crystallization process of $MAPbI_3$ thin film, retard the formation of perovskite film, and enhance crystallinity, absorption, and coverage on planar substrate uniformity (Diau et al. 2018). Besides the Cl-based additives, the MA-based additives also control perovskite morphology. A small amount of excess MAI mixed with standard PbI_2-MAI solution can grow 1-2 μm grain size with much better crystallinity, surface morphology, charge carrier lifetime and suppress non-radiative recombination, which is often beneficial for improving electronic properties and PSC device performance (Jung et al. 2019). Because excess MA cation compensates for the loss of MAI during the coating and annealing processes and suppresses the PbI_2 formation, it results in enlarging the nanometer perovskite crystal (Diau et al. 2018).

We reviewed the fabrication process of $MAPbI_3$-based perovskite materials by investigating solvent engineering, chemical concentration and additives, deposition, and the coating method. We summarized that to produce large-scale perovskite film, we needed to use the blade-coating technique. In addition, the one-step deposition method is easier and more convenient to transform PbI_2 to $MAPbI_3$. Furthermore, additional MAI and MACl improves perovskite film surface morphology, crystal size and uniformity. Thus, as a result of the literature review, we

decided to divide the thesis into two parts, first being to investigate the binary solvent (mixed

concentration of DMF and DMSO) and test samples of electronic and physical properties. Later,

we used the optimized solvent ratio from the first part and added additional MA cation to the

precursor solution, and we did the same test for the second group. The perovskite samples were

fabricated with a 0.4 mol $MAPbI_3$ (63.6 mg MAI and 183.3 PbI_2, purely DMSO solvent)

precursor solution.

2.6 Solar cell devices

The perovskite solar panel works in a similar way to a traditional solar panel. A semiconductor

absorbs solar energy and converts it into electricity. The perovskite solar cell has five layers, as

shown in Figure 3, including indium tin oxide (ITO) substrate, an electron transport layer (ETL)

and hole transport layer (HTL), where the free electrons and holes are injected into, a perovskite

layer, and a metal contact. Depending on which layer (ETL or HTL) first encounters light rays,

the perovskite solar cell divides into two types, regular n-i-p structure (ETL deposit first and

encounters sunlight first) or p-i-n structure (HTL deposit first) (Sirbu et al. 2021).
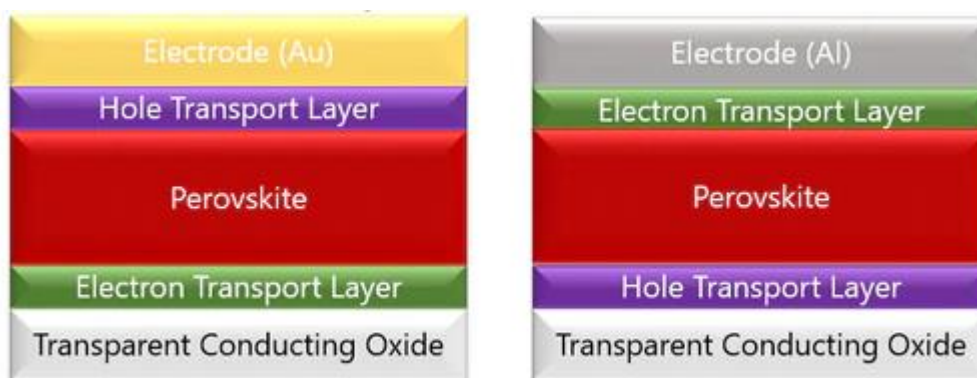
Figure 3. Structure of n-i-p (left) and p-i-n (right) perovskite solar cell (Sirbu et al. 2021)

Figure 4 below shows the p-i-n junction solar cell structure, which has a similar working process as a perovskite solar cell. Negatively charged acceptor ions exist within the p-layer together with holes that are induced by ionization of the acceptor atoms. The n-layer contains positively charged donor ions. Near the p-n junction interface at the center, the holes induced by acceptors and electrons generated by donors will recombine (Kita et al. 2018). Thus, a depletion region (perovskite layer) appears, which has no electrons and holes. Because the number of electrons and holes are the same, the charge maintains neutrality in the depletion region and there is a strong electric field. When a light ray is absorbed by the depletion region, the depletion will generate electron-hole pairs. Because the electron is a negatively charged particle, it is repelled by the acceptors and attracted by donor ions. Similarly, the hole is a positively charged and moves to the p-type region. Thus, there is more density of electrons in the n region and more holes in the p region (Kita et al. 2018). If we connect the n region and p region with a load (such as a lamp), a direct current will be generated.
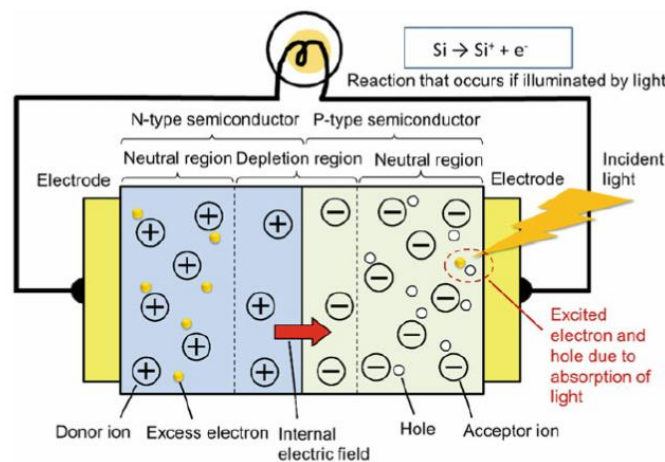
Figure 4. Schematic of the p-n junction solar cell structure (Kita et al. 2018)

To measure the perovskite solar cell device properties, we introduced the open circuit voltage and short circuit current. The short circuit current is the current generated when the terminals of

the solar cells are shorted; it is the maximum amount of current that is produced by a solar cell. The short circuit current density (J_{sc}) is expressed in mA/cm^2, and can be measured by the solar simulator device. The short circuit current density depends on the number of photons (the power of incident light source), the spectrum of incident light, and the optical properties (transmission and thermalization losses) (Kita et al. 2018). The current passing through a solar cell can be expresses as:

$$I_{sc} = J_{sc} \cdot A$$

Open circuit voltage is the maximum voltage available from a solar cell when the current is passing through is zero. The open circuit voltage depends on the solar cell device temperature and the bandgap (E_g) (Levy & Christiana. 2006).

The short circuit current and open circuit voltage are the maximum current and voltage from a solar cell, but the power from both of these operating point is zero. The fill factor (FF) is a parameter that relates to V_{oc} and I_{sc}, determines the maximum power from a solar cell and can be expressed as:

$$FF = \frac{P_{mp}}{V_{oc}I_{sc}} = \frac{I_{mp}V_{mp}}{V_{oc}I_{sc}}$$

An FF is measure the 'squareness' of the $I - V$ curve, thus a solar cell device with higher voltage is more likely to obtain a higher FF. The maximum FF from a solar cell can be found via differentiating the power respect to voltage to zero:

$$\frac{d(IV)}{d(V)} = 0$$

The *FF* can be represented as the ratio between the blue and green rectangular areas shown

below:
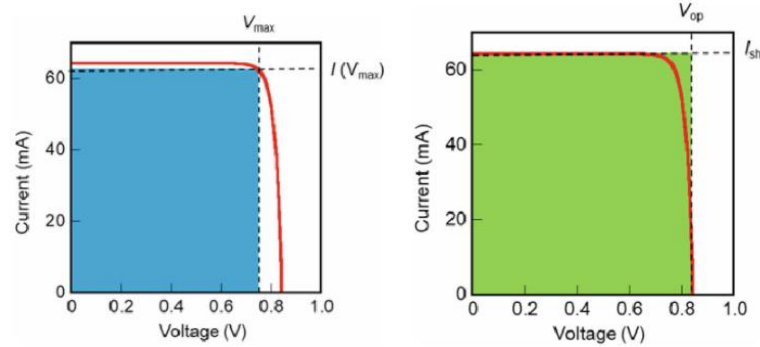
Figure 5. Product of Vmp and Imp (left), Product of Voc and Isc (right) (Kita et al. 2018)

The most relevant figure of merit is the power conversion efficiency (PCE) of a solar cell and is

defined as the ratio of energy output from the solar cell to input energy from the sun. The PCE

depends on the spectrum and intensity of the incident sunlight and the temperature of the solar

cell (Honsberg & Bowden. 2019). The PCE is expressed as:

$$\eta = \frac{P_{max}}{P_{in}} = \frac{V_{oc}I_{sc}FF}{P_{in}}$$

Where P_{in} is the incident light power.

2.7 Light concentrators

Solar cell performance depends on the light radiation density upon the cell surface. More

sunlight shooting on the cell surface can significantly increase the solar cell efficiency (generate

more electrons and holes) and reduce the cell area (Alzahrani et al. 2021). Therefore, the

concentrator becomes an essential part of the concentration photovoltaic (CPV) system that

harnesses solar energy by increasing the solar density upon cells using optical concentrators (Alzahrani et al. 2021).

In addition, tunning the bandgap is one of the most important characteristics of the perovskite solar cell. Thus, perovskite material can be used in tandem or using a multi-junction solar cell (made by stacking several solar cells with increasing bandgaps on top of each other) to exploit a larger part of the solar spectrum and reduce the thermalization losses (Philipps et al. 2014).

In this study, we focused on non-tracking concentrators that were easier to evaluate.

In general, a solar concentrator consists of mirrors and lenses that can concentrate incident light and redirect the light propagation to the receiver. Some of the benefits and drawbacks of using concentrators are:

Benefits:

- Reduces the materials needed in the solar junction.
- Increases the intensity of solar irradiance to increase the solar cell conversion efficiency.

Drawbacks:

- Degrades the PV cell lifespan because of heat/light focusing
- Usually requires expensive systems with tracking included

Types	Description
Reflector	Upon hitting the concentrator, the rays will reflect to the PV cell. e.g: Parabolic Concentrator
Refractor	Upon hitting the concentrator, the rays will refract to the PV cell. e.g: Fresnel Lens Concentrator
Hybrid	Upon hitting the concentrator, the rays can both refract and reflect before hitting the PV cell. e.g: Dielectric Totally Internally Reflecting Concentrator
Luminescent	The photons will experience TIR and guiding to PV cell. e.g: Quantum Dot Concentrator

Table 1. Types of Light Concentrators (M, S, Firdaus. 2010)

The most widely used concentrator is the Compound Parabolic Concentrator (CPC), which has a large acceptance angle (non-tracking) and achieves uniform concentrated light at the absorber to avoid too much heat on the cell surface. Thus, we focused on the reflector type concentrator.

The concentration ratio characterizes the light concentration process: It is the factor by incident energy flux(I_0) that is optically enhanced on the receiving surface (I_r). The geometric concentration ratio is given by:

$$C_{geo} = \frac{A_a}{A_r}$$

Where A_a is the area of aperture and A_r is the receiver area. Figure 6, shown below, indicates the relationship between A_a and A_r.
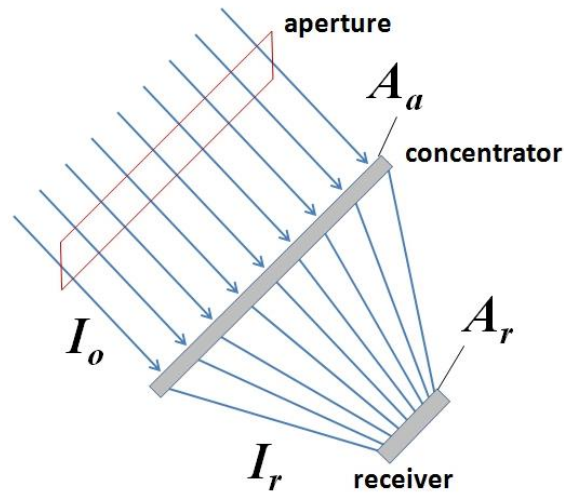
Figure 6. Concentration Ratio Indication.

The compound parabolic concentrator (CPC) can collect the most sunlight (both beam and diffuse) and redirect it to the receiver. The CPC does not need a specific incident angle of light. A CPC consists of two segments of parabolas and each parabola has its focal point at the lower edge of the opposite side parabola mirror. For example, Figure 7 shows that the CPC has two parabola segments, AC and BD. The AC parabola segment collects the light to B and the BD concentrates light to A. Then, the receiver can be located between A and B.
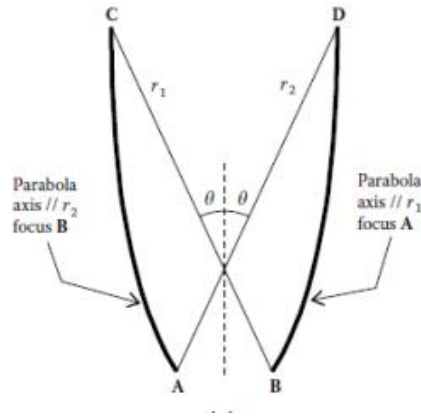
Figure 7. Geometry of a CPC
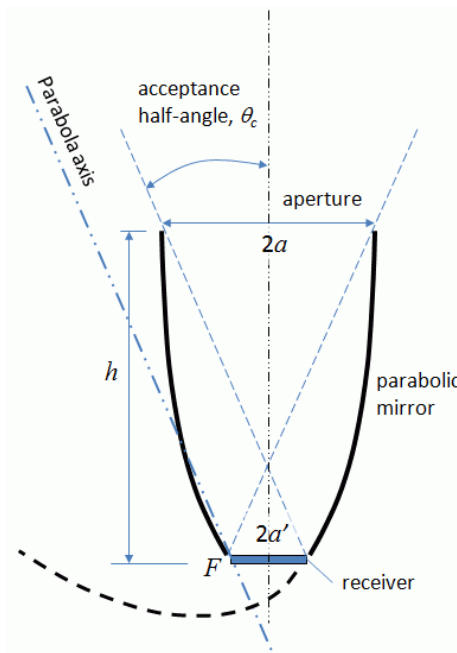
Figure 8. Schematic of compound parabolic concentrator

To design the CPC, we needed to determine the parameter a, a', h and θ_c. Where $2a$ is the area

of aperture, $2a'$ is the area of the receiver, h is the height of concentrator and 'θ_c' is

the acceptance half-angle. The relation between the area of aperture ($2a$), the area of the receiver

(2a') and the acceptance half-angle (θ_c) is:

$$2\alpha' = 2\alpha\sin(\theta_c)$$

Then, from the equation of concentration ratio, the relation is shown below:

$$C_{geo} = \frac{2\alpha}{2\alpha'} = \frac{1}{\sin(\theta_c)}$$

The following equations relate the focal distance of the side parabola (f) to the acceptance angle, receiver size, and height of the collector:

$$f = \alpha'(1 + sin\theta_c)$$

$$h = \frac{fcos\theta_c}{sin^2\theta_c}$$

The incident angle greater than the acceptance half-angle (θ_c) will not be received by the receiver and it will be reflected to the aperture. The angle of incident light that is smaller than the acceptance half-angle will reach the receiver. Figure 9, shown below, indicates these three situations.
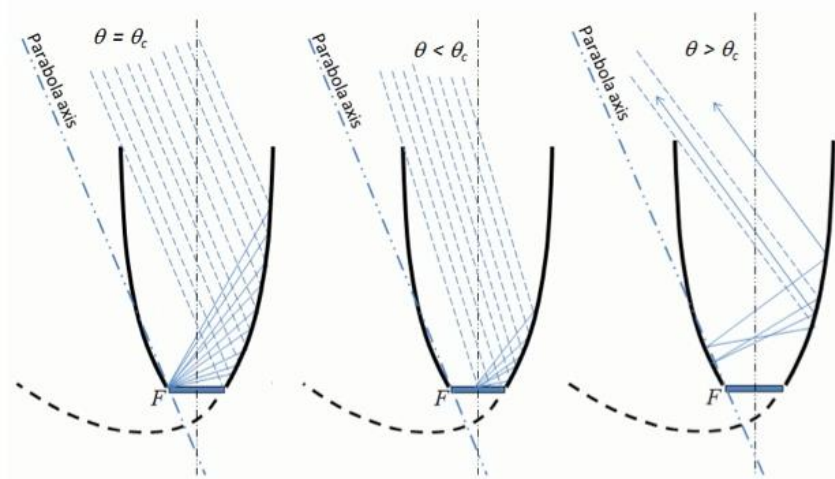
Figure 9. Relationship between incident angle and acceptance angle.

The Compound Parabolic Concentrator offers a higher geometrical concentration gain with a narrow field of view. However, it requires a tracking system to maximize the collection of sun radiation. A CPC Trough is a type of CPC. It is designed by length and height instead of a circular aperture. The design parameters are the same as a CPC. Figure 10 shows the 3D model of a CPC Trough.
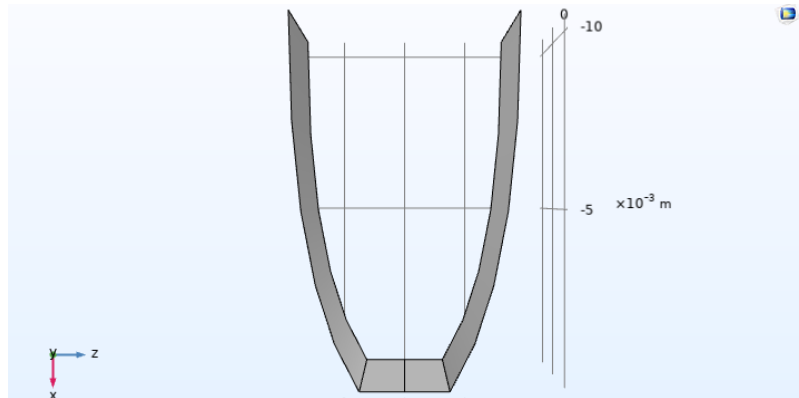
Figure 10. 3D model of Compound Parabolic Concentrator Trough.

A DPT is a combination of two CPC troughs. In this simulation, we designed one parabolic trough tilted 8 degrees and another one tilted -8 degrees. The intercept of the two parabolic troughs is a block type absorber. The absorber can be vertical or horizontal to the bottom. Figure 11(a) shows the vertical type of absorber DPT, and Figure 11(b) shows the horizontal type of absorber DPT.
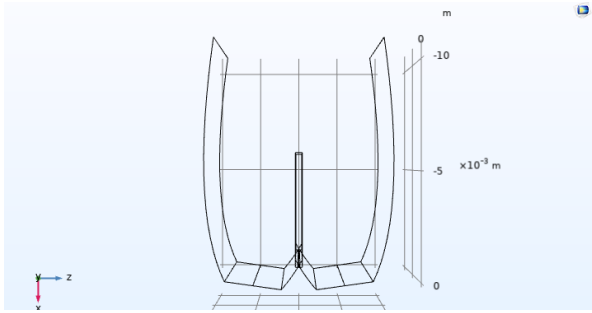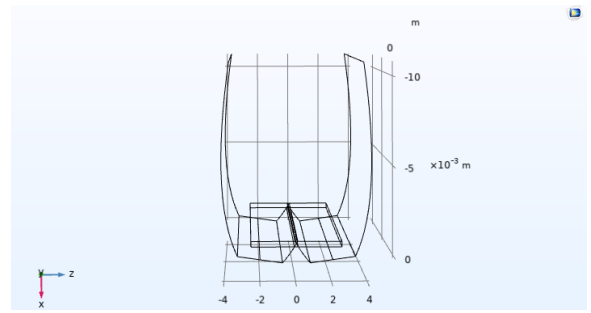
(a)   (b)

Figure 11. Two type absorbers of DPT (a) DPT with vertical absorber. (b) DPT with horizontal absorber.

CHAPTER 3 Experimental

3.1 Materials

Mthylammonium Iodied (MAI, >98.0%), methylammonium chloride (MACl, >98.0%), and lead (II) iodide (PbI2, 99.99%) were purchased from TCI. Poly solvents, such as dimethylformamide (DMF), dimethyl sulfoxide (DMSO) were obtained from Alfa Aesar.

3.2 Perovskite samples and device simulation

3.2.1 Perovskite samples fabrication

The patterned ITO substrates were ultrasonically cleaned using deionized water (DI-H_2O) and a few drops of 'Triton' detergent for 20 minutes. They were cleaned with pure DI-H_2O, Acetone, and Isopropyl alcohol (IPA) for 20 minutes each. The substrates were then dried using a nitrogen gun, and effective organics were removed using UVO cleaner for 20 minutes.

After the substrate was cleaned and dried, the active layer was ready to deposit. The blade precursor solution was prepared by dissolving 184.4 mg PbI_2 and 63.6 mg MAI in 1 mL of DMF-DMSO solvent mixtures of varying volume ratios under stirring at 400rpm, 70℃ for 7 hours. The resulting solutions were spread onto prepared substrate on a 150℃ hotplate with 0.1mm/s blade moving speed and left for 2-4 minutes to dry (too much time will burn, and less time will degrade the samples during transport). Then, the samples were quickly transferred to a glovebox to avoid moisture and were annealed for 20 minutes at 130 ℃. After we obtained the best solvent ratio of DMF-DMSO, we changed the concentration of MAI and MACl from 1 to

1.3 mole and 0.05 to 0.2 mole, respectively, to obtain high-quality film.

3.2.2 Perovskite solar cell simulation parameters

The perovskite solar cell device has five layers, as discussed in chapter 3, and the solar cell

performance depends on the quality of perovskite film. Thus, investigating the thickness and

electronic properties of the active layer is important. The SCAPS simulation software solves the

semiconductor-based Poisson's equation and continuity equation at defined boundary conditions

(Aseena et al. 2021) and it efficiently demonstrates the perovskite solar cell performance. The

device was designed with 0.02μm thickness ETL and 0.09μm HTL as optimum values for

perovskite-based cells (Aseena et al. 2021), and the active layer had variables from 0.4 to

1.9μm. The absorption data was obtained from the perovskite samples. We obtained the material

parameters from various literature as shown in Table 2. The active layer's defects density

changes the optoelectrical properties of a material system and has lots of challenges that are not

available in many groups. Therefore, investigating the influence of the defect density in active

layers and the layer interface between perovskite/HTM, and ETM/perovskite were the primary

purposes of this simulation. The absorb layer's defect density and the interface layer's defect

density are considered the variables and are obtained from literature and shown in Table 3.

Material Parameters	ZnO	$Ch_3NH_3PbI_3$	Sprio-OMeTAD
Thickness(nm)	20		90
Bandgap(eV)	3.3	1.55-1.6	3.17
electron affinity (eV)	4	3.9	2.05
dielectric permittivity (relative)	9	10	3
CB effective density of states (1/cm^3)	2E18	2.75E18	2.2E18
VB effective density of states (1/cm^3)	1.8E19	3.9E18	1.8E19
Electron/Hole thermal velocity (cm/s)	1E7	1E7	1E7
electron mobility (cm²/Vs)	100	10	2E-4
hole mobility (cm²/Vs)	25	10	2E-4
Nd	1E18	1E9	0
Na	NA	1E9	1E19
Nt	1E15	NA	1E15

Table 2. Material parameters of different layers (Aseena et al., 2021)

From literature, we knew the MAPbI$_3$ trap density is 1.59×10^{16} cm^{-3} with the spin-coating method (Xiao et al. 2021). The film that incorporated excess MA cations can reduce the trap

density to 8×10^{14} cm^{-3} (Wang et al. 2018), which can conclude both the MAI and MACl study. The interface defect density between ETL/Perovskite could be decreased from 10^{16} to 10^{11}. Considering the barrier of coating technique, the blade coating has a rougher surface and larger crystal size, so the defect density will be changed according to film quality.

Parameters	ETM/Perovskite interface	Perovskite layer	Perovskite/HTM interface
Defect type	Neutral	Neutral	Neutral
Capture cross-section for Electrons and holes/cm^2	1×10^{-19}	1×10^{-15}	1×10^{-19}
energetic distribution	single	single	single
energy level with respect to Reference (eV)	0.6	0.6	0.6
Total defect density (cm^{-3})	$1 \times 10^{11-16}$	$1 \times 10^{11-17}$	$1 \times 10^{11-16}$

Table 3. Parameters for interface defect layers and absorber

3.3 Characterization

An optical microscope was used to investigate the quality of samples' morphology and find out the crystallinity for each sample. Because of the resolution of an eye (the human eye can distinguish two points with 0.2 mm space), many structures can no longer be characterized by light microscopy. Thus, we use scanning electronic microscope (SEM) to obtain further characterization of the samples. The scanning electronic microscope (SEM) projects and scans a focused stream of electrons over a surface to create an image with much shorter wavelengths, which enables better resolution.

Ultraviolet-Visible (UV-Vis) spectroscopy was used to measure the absorption properties of samples with wavelengths from 0.3µm to 0.8µm. The absorption spectra were obtained from Agilent Cary 7000 with the Cary Scan software program. The confocal laser scanning microscopy (CLSM) was used to measure the film thickness via the pinholes on the film surface. Once the absorbance and thickness of films was obtained, we used Tauc plots to draw and calculate the sample's bandgap.

Photoluminescence (PL) is when light energy or photons is directed onto a sample, and when it is absorbed, a process called photoexcitation can occur. This process causes the electron to jump to a higher state. Because the electrons are not stable in a higher-level state, they will release energy and fall back to the ground state. The emission of light or luminescence during this process is photoluminescence. PL spectroscopy can characterize the optical and electronic properties of perovskite film, and the model of the instrument we used is a Cary eclipse fluorescence spectra meter.

X-ray diffraction (XRD) is based on the bending of light around the corner of an obstacle. The XRD instrument can measure the crystal within a few angstroms (approx. 1Å), the degradation of the perovskite sample, and the crystal orientation of thin films by Bragg's law, and can be calculated by following equation:

$$2d \sin \theta = n\lambda$$

Where d is the spacing between two particles, λ is the wavelength of radiation, θ is the angle between the incident (or diffracted) ray, n is an integer, referred to as the order of diffraction, and is often unity.
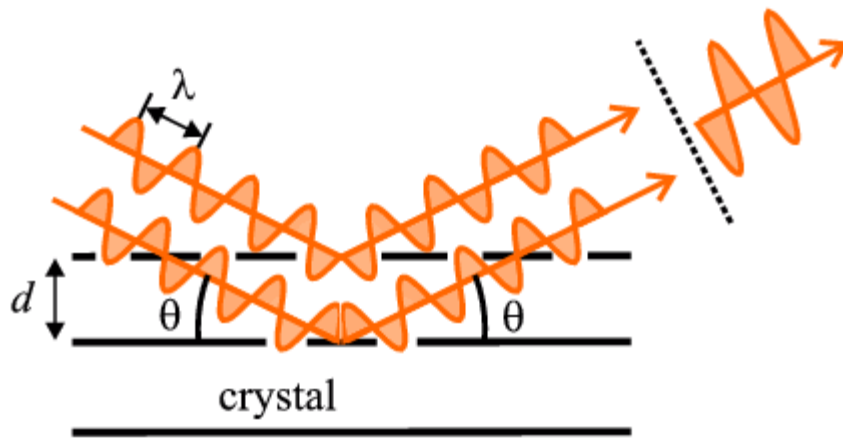
Figure 12. Schematic of Bragg's law

An LCR meter is a type of electronic test equipment used to measure the electronic properties such as the impedance (Z), inductance (L), capacitance (C) and resistance (R) of a component. The LCR meter IM3536 offers a wide DC and frequency (we tested the film from 4Hz to 100000Hz), and the test fixture was 9261-10.

Fourier transform infrared (FTIR) spectroscopy is a technique used to obtain the infrared spectrum of absorption, emission, and photoconductivity of samples (Pandey, A. et al., 2015). A FTIR spectrometer includes a source, sample cell, detector, amplifier, A/D convertor, and a computer. Radiation from the sources reaches the detector after it passes through the interferometer. The signal is amplified and converted to a digital signal by the A/D convertor and amplifier, after which the signal is transferred to the computer, where the Fourier transform is carried out (Shukla et al. 2017). We used the mid-IR region (between 5000 cm^{-1} and 400 cm^{-1}) to test the film by using the instrument Cary 630 FTIR.

The solar simulator works as an equipment employing a light source with a spectral distribution

similar to the natural sunlight used to evaluate characteristics of PV devices, such as the V_{oc} and J_{sc}. Therefore, the solar simulator is an artificial light source which can simulator the sunlight with similar intensity and wavelength of sunlight. The solar simulator and fabricated PSC device used in this experiment is shown in appendix.

CHAPTER 4   Results and Discussion

4.1 Perovskite electronic properties

All active layers were coated using the blade-coating method at 150 ℃ hotplate, 0.1 mm/s blade moving speed, and 200 µm gap between blade and hotplate. The entire process of fabrication needed a dry air atmosphere and 15%-20% of relative humidity.

4.1.1 Mixed solvent

In this work, the morphology characterization of the perovskite film was carried out by SEM and OM. From OM images, we obtained the optimal crystal size using an 8:2 (DMSO: DMF) solvent mixture followed by 9:1 (DMSO: DMF). The 7:3 (DMSO: DMF) solvent mixture shows the smallest crystal size. As the DMF was added, the surface of the perovskite film became smooth. Interestingly, when the solvent mixture reached 7:3 (DMSO: DMF), the uneven surface came out, which agreed with the OM images.

(a)　　　　　　　　　　　　　　　　　(b)

10.0kV 13.5mm x250 SE(M)　　　　　200um　　10.0kV 13.5mm x250 SE(M)　　　　　200um
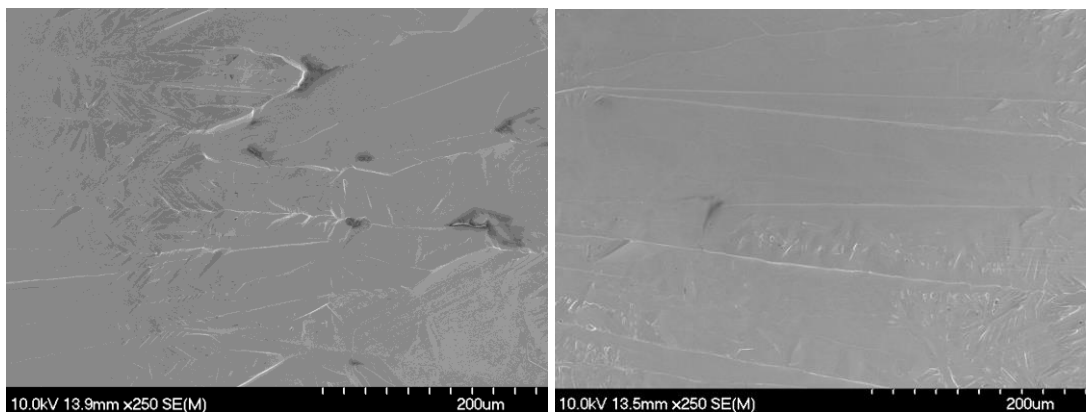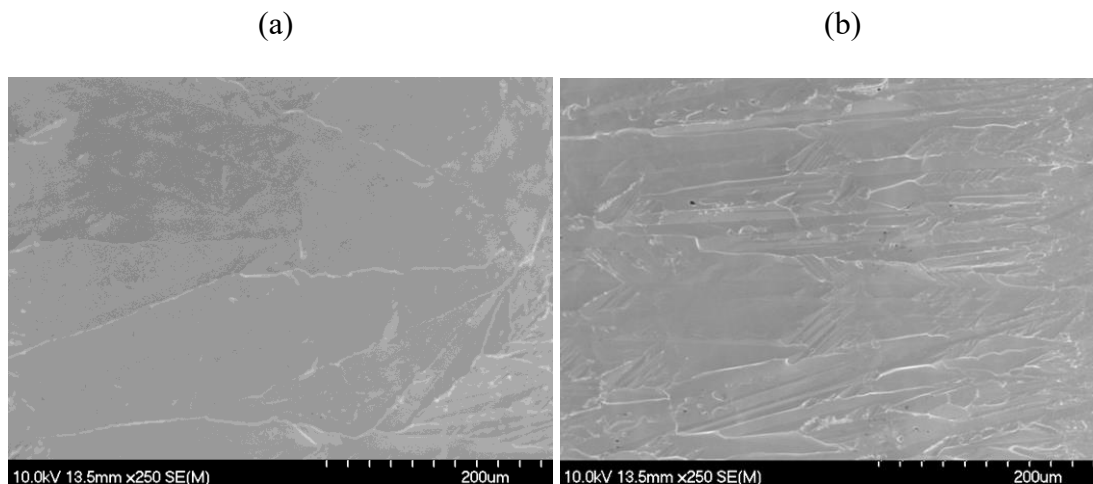
(c)　　　　　　　　　　　　　　　　　(d)

Figure 13. SEM images of solvent study. (a) DMSO: DMF (10:0), (b) DMSO: DMF (9:1), (c) DMSO:DMF (8:2), (d) DMSO:DMF (7:3)

(a)　　　　　　　　　　　　　　　　　(b)

(c)	(d)
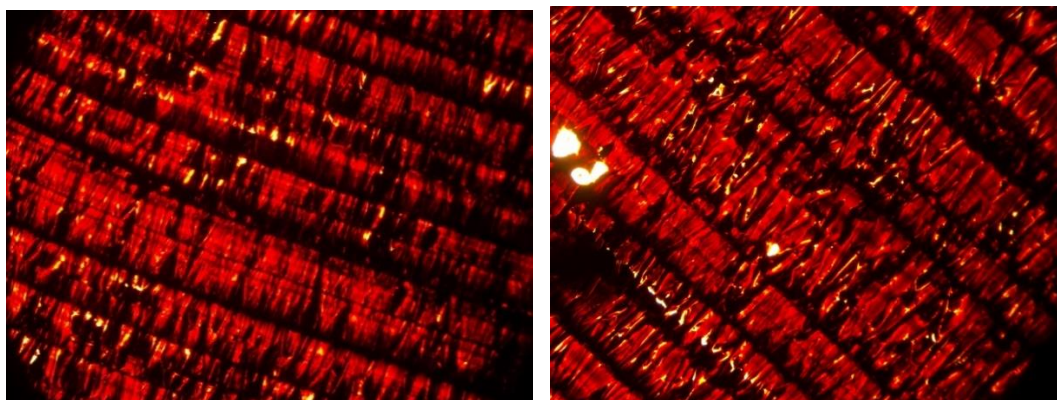
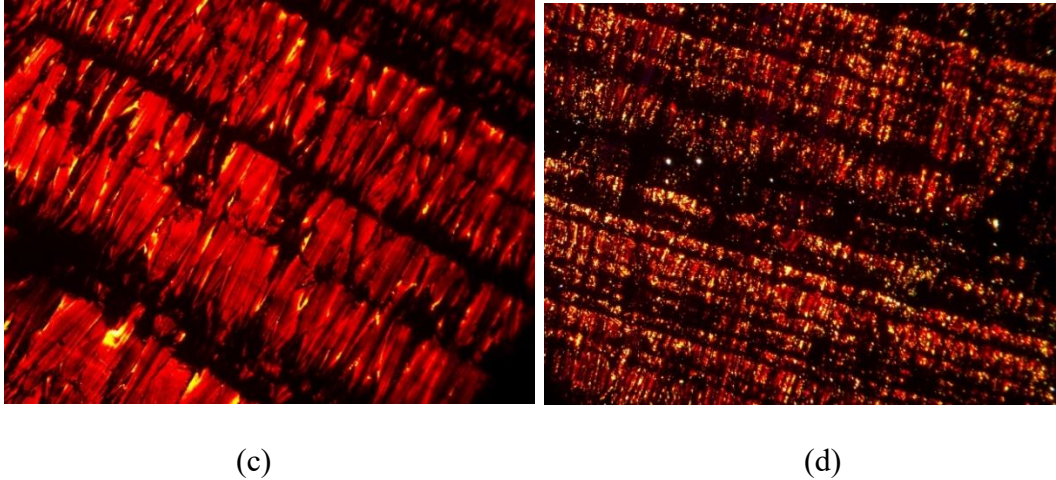*Figure 14. OM images of solvent study. (a) DMSO: DMF (10:0), (b) DMSO:DMF (9:1), (c) DMSO:DMF (8:2), (d) DMSO:DMF (7:3)*

Table 4 and Figure 15 (a) show the thickness and bandgaps of the perovskite layer respectively. The thicknesses (from 1.8μm to 1.9 μm) and the bandgap (1.57 to 1.58 eV) stayed in the same range because the bandgap and absorbance depend on the thickness of the active layer. From Figure 15 (b), we see that all the samples displayed absorption onset at ≈780 nm with a sharp raise at ≈740 nm, which can effectively characterize the formation and bandgap absorption of MAPbI$_3$. The absorbance graph showing the mixed solvent ratio with 8:2 (DMSO: DMF) had the highest absorbance, followed by 7:3 and 10:0, and the lowest absorbance was 9:1 ratio DMSO: DMF. The PL spectrum showed an emission peak was centered between 0.78μm and 0.81μm and slightly changed when the solvent ratio changed. The shift of the emission peak could be the result of poly solvent concentration changes. Interestingly, the absorbance of the 9:1 (DMSO: DMF) ratio was the lowest, but the PL intensity was as high as 8:2 solvent ratio. The reasons could be the surface roughness and crystal formation not being homogeneous.

Solvent ratio (DMF: DMSO)	Sample thickness
0DMF:10DMSO	1.9um
1DMF:9DMSO	1.82um
2DMF:8DMSO	1.92um
3DMF:7DMSO	1.91um

Table 4. The active layer thickness of different solvent ratios

(a)   (b)

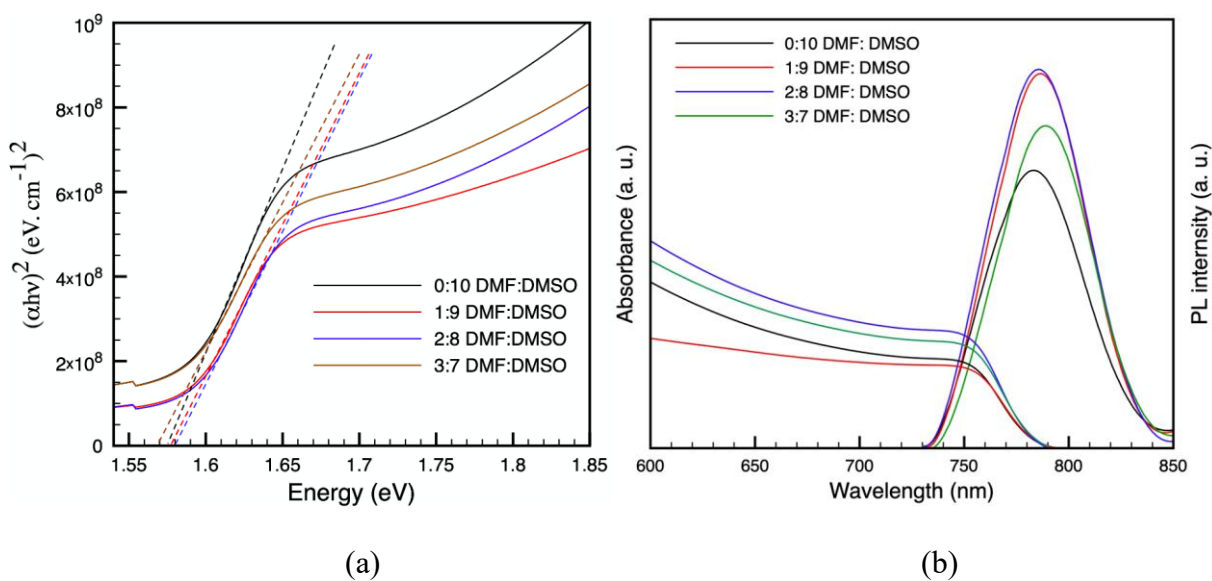*Figure 15. The (a) bandgap, (b) absorbance, and PL spectra of MAPbI3 mix solvent films*

The impedance - frequency spectra, especially in the lower frequency range, showed lower impedance values for 2:8 followed by 1:9 then 3:7 and 0:10. The impedance here was the observed impedance, which is the complex impedance containing both the real and the imaginary parts. The impedance can be calculated by the following formula:

$$Z = \frac{R}{1 + j\omega RC}$$

Where $\omega = 2\pi f$, R is the resistance, and C is the capacitance.
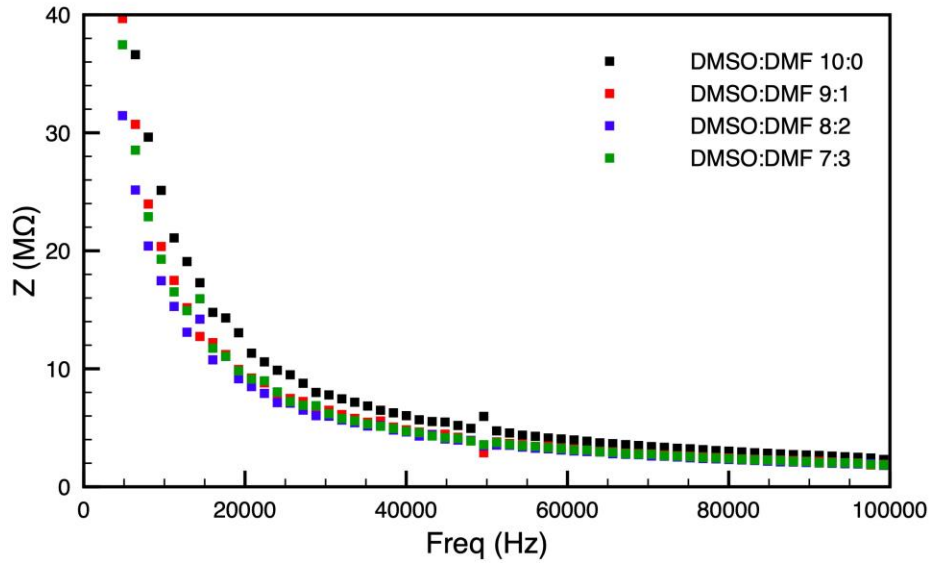
Figure 16. Impedance of MAPbI3 perovskite thin film with mixed solvent

Figure 17 shows the IR spectra for the chemical structure of $CH_3NH_3PbI_3$ particles in solvent. The typical peaks of O-H and N=C=S stretching for perovskite could be identified around 3180 and 2090 cm^{-1}. The C-H bending and C=C bending could be observed at wavenumber 1465 and 710 cm^{-1}, respectively. Such results agreed with the conversion results.
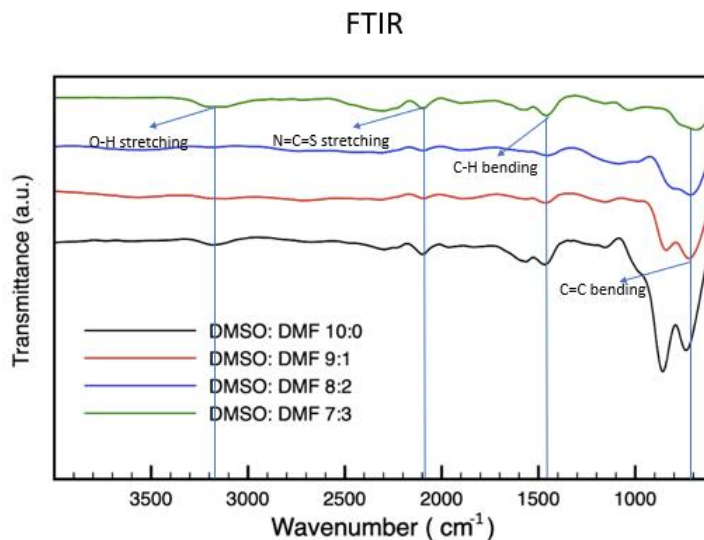
Figure 17. FTIR spectra of mixed DMF: DMSO solvent perovskite films

4..1.2 Role of MAI

From the solvent study, we summarized the optimal solvent ratio is 2DMF: 8DMSO. Thus, to

investigate the effect of MAI, we fabricated the perovskite film with MAI: PbI_2 (1:1) and the

solvent ratio DMF: DMSO (2:8) as the controlled sample. Then, we increased the MAI

concentrations from 1 to 1.5 mol. From SEM images, when additional MAI with 0.2 mol was

added, it showed the smoothest surface with the least pinholes (the black spots in Figure 18 (a),

(b) are suggested to be the pinholes of the film). Interestingly, with more MAI added to the

precursor solutions, the white clusters can be seen around the grain boundaries as shown in

Figure 19 (d), which could be the residue of MAI that showed an incomplete reaction with PbI_2

to form the crystals. The OM images showed the film with 1.2 MAI concentration had the least

pinholes and smoothest surface, which agreed with SEM images. Figure 18 (d) showed that the

31

formed crystal with the chemical concentration ratio of 1. 3MAI:1PbI2 started to crash, since too much MAI affects the bonds between MAI-PbI$_2$, but the crystal size relatively increased due to the compensation of losses MAI during the shearing and annealing process (Diau et al. 2018).
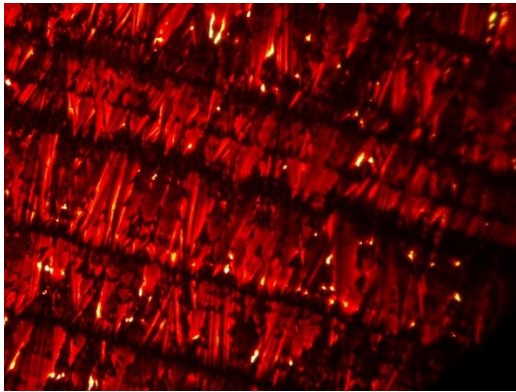
(a)
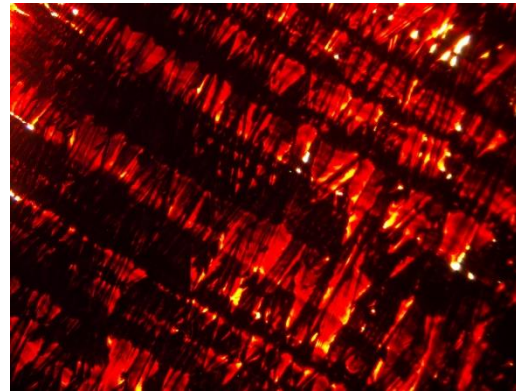
(b)
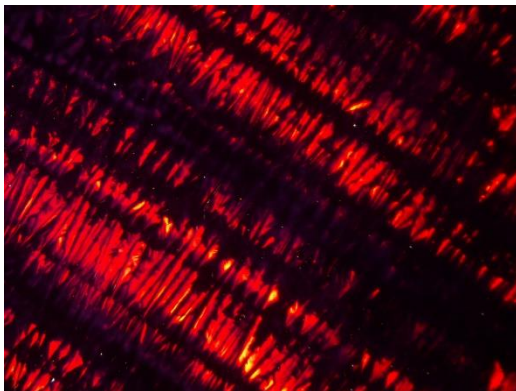
(c)
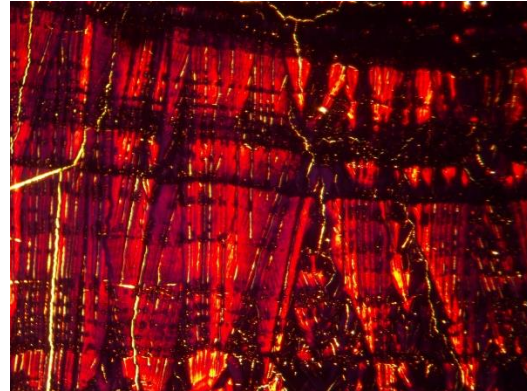
(d)

Figure 18. OM images of exceed MAI. (a) MAI: PbI2 (1:1), (b) MAI: PbI2 (1.1:1), (c) MAI: PbI2 (1.2:1), (d) MAI: PbI2 (1.3:1)
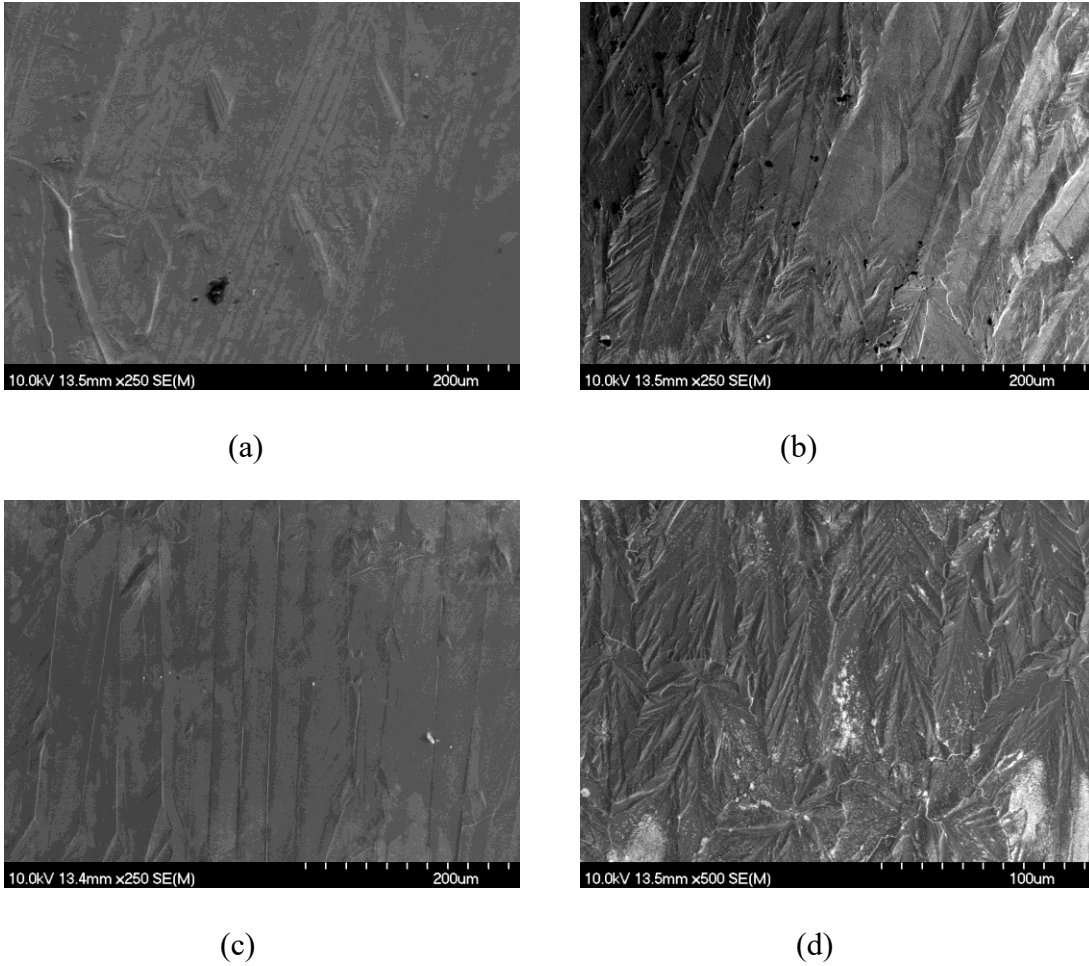
Figure 19. SEM images of exceed MAI. (a) MAI: PbI2 (1:1), (b) MAI: PbI2 (1.1:1), (c) MAI: PbI2 (1.2:1), (d) MAI: PbI2 (1.3:1)

Table 5 shows the perovskite film thickness with various MAI added to the precursor solution. It obviously shows the thickness increased with the increased concentration of MAI and it reached the peak (2.12μm) when 1.4 mol MAI was added. Then, the thickness was reduced with 1.5 mol of MAI. The bandgap shown in Figure 20 (a) indicates the excess MAI slightly changed the bandgap due to the changing of thickness. The thickness increased and the bandgap reduced. In addition, the 1.2 mol MAI additive showed the highest absorbance with great crystal morphology, fewer pinholes, and similar thickness compared with the controlled film. Figure 20 (b) shows the PL spectra and UV-Vis absorbance of the MAPbI3 films with different MAI

concentrations. The peak position of the PL spectrum increased from 788 to 795 nm and higher

absorbance was observed when the MAI concentration increased from 1 to 1.1 mol. It reached

the highest PL intensity (790 nm) and absorbance when 1.2 mol MAI was added. The peak of

the PL spectrum had a redshift because of the increase in the MAI concentration (789, 786, and

783nm with 1.3, 1.4, and 1.5 mol MAI added, respectively), which also could be observed from

the absorbance graph. The shift might have been associated with the reaction of PbI_2 and MAI

(Li et al. 2016), and the formation of slightly larger particles (Zhang et al. 2019). The

absorbance with 1.3, 1.4, and 1.5 mol MAI added was lower than the controlled film, and that

could have been the reason for surface roughness, crystal size, and the effect of residue MAI.

Chemical ratio	Sample thickness (um)
1MAI:1PbI2	1.92
1.1MAI:1PbI2	1.93
1.2MAI:1PbI2	1.96
1.3MAI:1PbI2	1.99
1.4MAI:1PbI2	2.12
1.5MAI:1PbI2	1.92

Table 5. The thickness of MAI study

(a) (b)
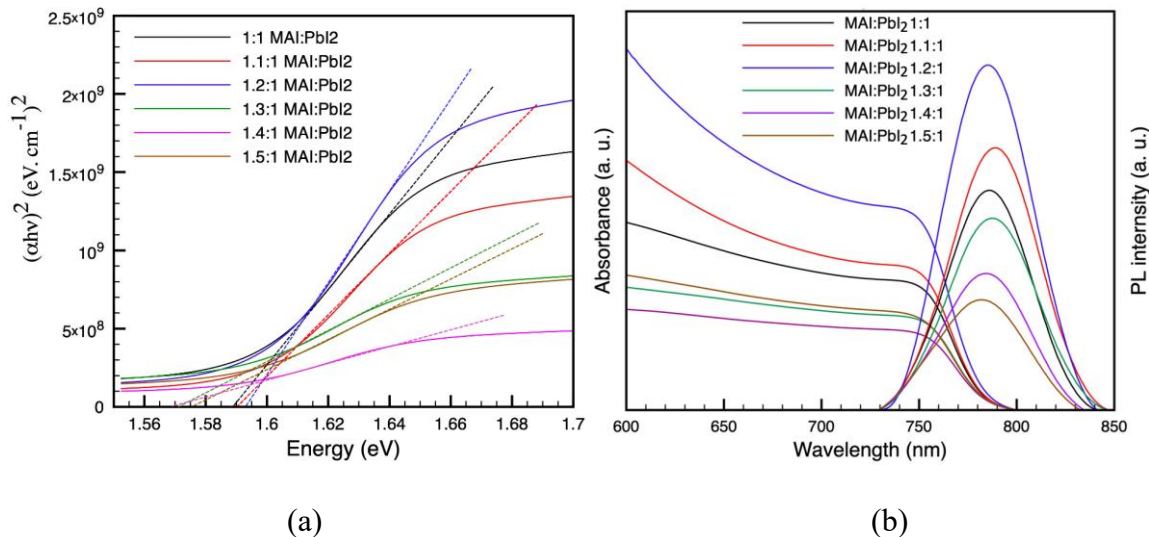
Figure 20. The (a) bandgap, (b) absorbance, and PL spectra of excess MAI perovskite films

Figure 21 showed the lowest impedance, especially in the low frequency range, with MAI: PbI$_2$ (1.2:1) followed by 1.3:1, 1.1:1 and 1:1. The impedance contained both real and imaginary parts. The real part is the resistance, and the imaginary part (capacitance and inductance) is the property to change the current flow. Thus, the lower impedance would have shown better performance on solar cell devices due to the larger current flow.
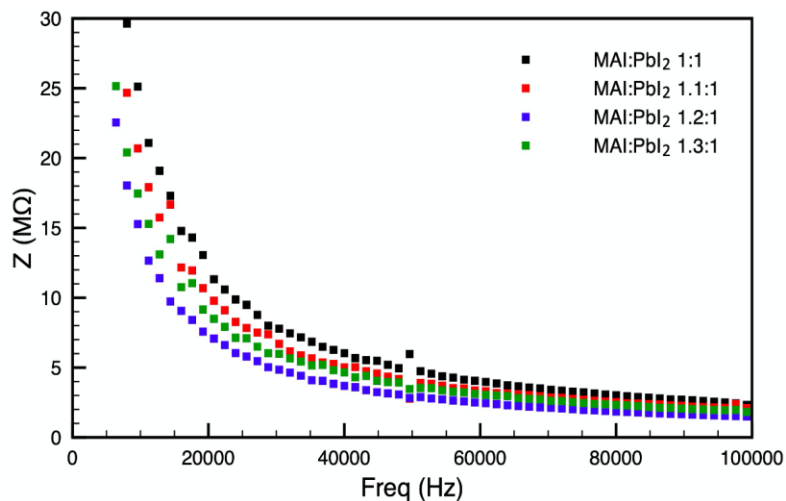
Figure 21. Impedance of MAPbI3 perovskite thin film with excess MAI

35

Figure 22 shows the IR spectra for the chemical structure of $CH_3NH_3PbI_3$ particles with excess MAI. The results are similar to FTIR in the solvent study, and it is considered that they have the same properties and chemical bonds' weakness in the IR region. However, the MAI: PbI_2 ratio with 1.3:1 and 1:1 showed only one peak at range from 900 to 700 cm^{-1}.
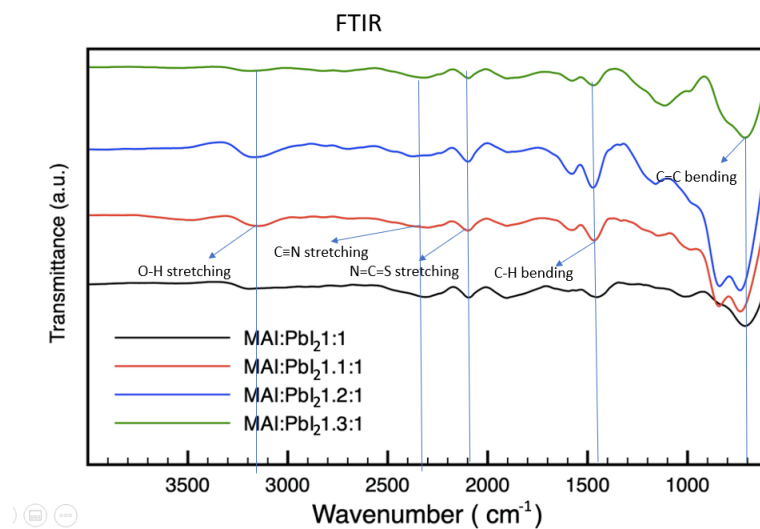
Figure 22. FTIR spectra of excess MAI perovskite films

4.1.3 Role of MACl

From the previous section, we summarized that the additional 20% of MAI efficiently grew the crystal size, reduced the impedance, and improved the absorption, which could mean better performance for device application. In this section, we added the MACl into the precursor solution (DMF: DMSO (2:8), MAI: PbI_2 (1.2:1)) from 0.05 to 0.2 mol and measured the optoelectrical properties.

By tuning the incorporation of MACl, the perovskite film quality can be significantly changed. The OM images showed the perovskite film with 0.05 mole MACl added had much larger crystals than the perovskite film without the MACl additive. From SEM images, the 0.1 mole MACl additive showed an optimized crystal size and surface roughness. However, the formed crystal got split at grain boundaries and it got worse with the 0.2 mole MACl additive. The reason could be the crystal shrink during the anneal process (the process may need a higher temperature). Obviously, the general crystal size with MACl additive is much larger than the film without MACl.

(a)

(b)

(c)

(d)

(a)

(b)

(c)

(d)
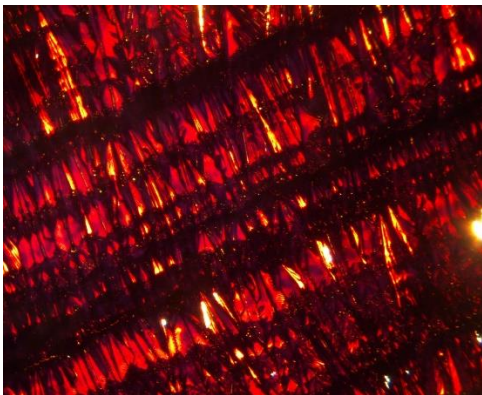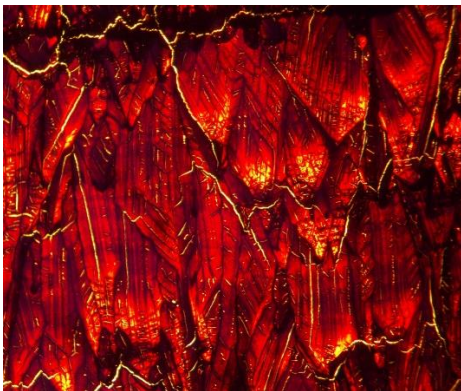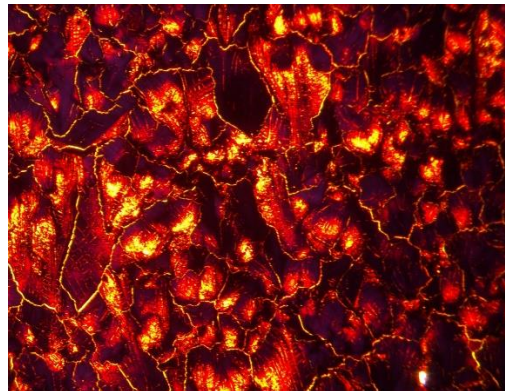
Figure 24. SEM images of MACl additive. (a) 0 MACl, (b) 0.05 MACl, (c) 0.1 MACl, (d) 0.2 MACl

Table 6 shows the thickness of perovskite samples was increased with more MACl concentration, but the bandgap had no significant change and remained in the range of 1.58 to 1.59 eV. The absorbance with 0.05 and 0.1 mol additional MACl had the same range and slightly enhanced the absorption compared with the controlled one. However, the perovskite film with 0.2 mol MACl added showed the most thickness but the lowest absorbance. The reason could be the crystal split at grain boundaries and the grain size. The main reason could be the retarded formation of perovskite film and the thicker perovskite layer (Guo et al. 2021). The

peak position of the PL spectrum is located around 790 nm and the intensity is increased by

adding more MACl. Thus, the radiative recombination rate was enhanced with the concentration

of MACl.

Chemical concentration	Thickness (um)
0MACl	1.96
0.05MACl	2.19
0.1MACl	2.34
0.2MACl	2.56

Table 6. The thickness of MACl additive
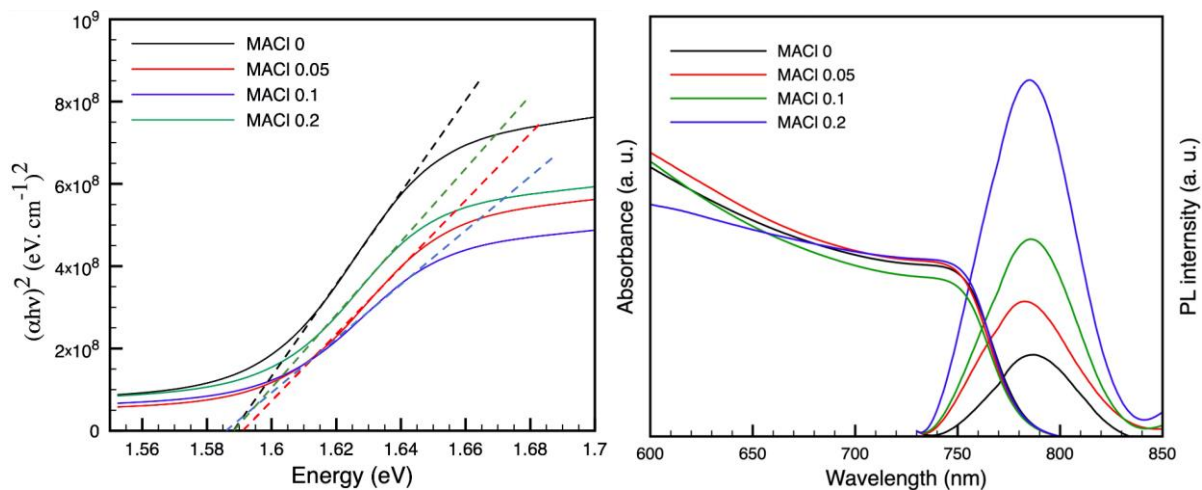
Figure 25. The bandgap (left), absorbance and PL spectra (right) of MACl additive MAPbI3 films

Figure 26 shows the impedance spectrum of additional MACl. The 0.1 mole MACl additive

showed the lowest impedance (3MΩ) in low frequency range followed by 0.05 mole, then 0.2

and the controlled one. Compared to the impedance in the solvent study and the excess MAI in the low frequency region (10000 frequency), the mixture solvent with DMF: DMSO (2:8) showed the lowest impedance around 16 MΩ and the excess MAI has around 13.5 MΩ. Thus, the MACl additive could have better performance on solar cell devices.
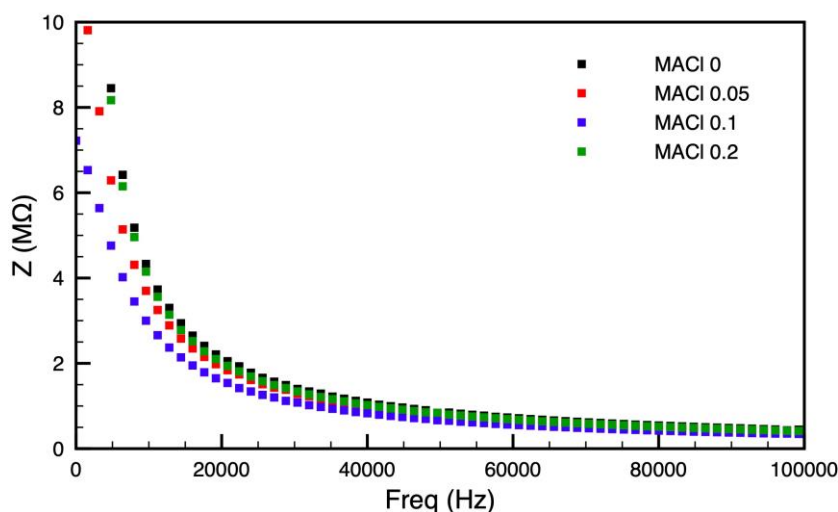
Figure 26. Impedance of MAPbI3 perovskite thin film with additional MACl

Figure 27 shows the IR spectra of various MACl concentrations in perovskite film. The peaks were centered around 720 cm^{-1}, 1465 cm^{-1} and 2100 cm^{-1} in all samples, which signalled presence of strong C-C bending, medium C-H bending and strong N=C=S stretching, respectively. The sample with 0.2 MACl added didn't show the peak centered around 3190 cm^{-1}, 810 cm^{-1}, which represented weak O-H stretching and strong C-H bending.
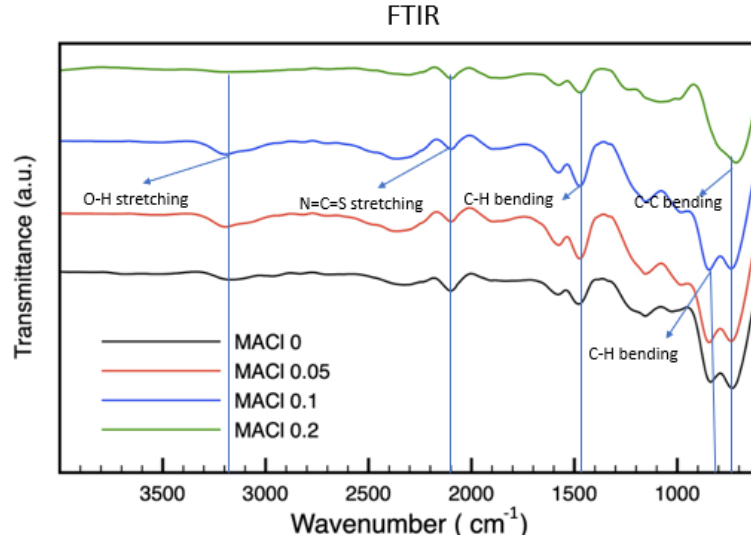
Figure 27. FTIR spectra of MACl additive perovskite films

4.2 Simulation approach

4.2.1 Perovskite solar cell simulation

The key characteristics of the optimized solar cell devices include the fill factor (FF), the open circuit voltage (V_{oc}), the short circuit current density (J_{sc}), and the power conversion efficiency (PCE) corresponding to perovskite layer defects, thickness, and layer interface defects.

We first investigated the perovskite layer defect from $1 \times 10^{11}\ cm^{-3}$ to $1 \times 10^{17}\ cm^{-3}$. The thickness and interface defects were fixed at 1.9μm and $1 \times 10^{16} cm^{-3}$. As seen in Table 7, the J_{sc}, V_{oc}, FF, and PCE did not change significantly since the perovskite layer density increased from 1×10^{11} to 1×10^{15} cm^{-3}. However, the defect density above 1×10^{15} cm^{-3} reduced the solar cell performance. These results agree with the literature review in Chapter 3 ($8 \times 10^{14} cm^{-3}$ is the threshold defect density).

Defect density	Thickness(μm)	J_{sc}(mA/cm^2)	V_{oc}(V)	FF (%)	PCE (%)
1×10^{11}	2	20.3	1	76	15.5
2.23×10^{13}	2	20.3	1	75.8	15.4
8.89×10^{13}	2	20.3	1	75.5	15.3
4×10^{14}	2	20.28	1	74.2	15
1×10^{15}	2	20.23	1	72	14.45
2.3×10^{16}	2	18.4	0.9	47.97	7.97
4.5×10^{16}	2	16.8	0.86	40.44	5.83
1×10^{17}	2	13.5	0.79	31.52	3.38

Table 7. Effect of MAPbI3 defect density on solar cell performance

Figure 28 illustrates the effect of thickness of the perovskite layer. The defect density of perovskite layer, ETL/Perovskite, and Perovskite/HTL are controlled. It can be observed that the active layer thickness has no significant effect on short current density (J_{sc}) and open circuit voltage (V_{oc}). The J_{sc} and V_{oc} reached the peak when the perovskite layer thickness was 0.75 μm and 1μm, respectively. However, with the thickness increased, the fill factor (FF) was reduced as a linear shape. The power conversion efficiency (PCE) increased since the active layer became thicker and reached the peak at 0.7 μm thickness with 14% efficiency. Then, it dropped rapidly with the thickness increase and the overall shape acting as a parabola.
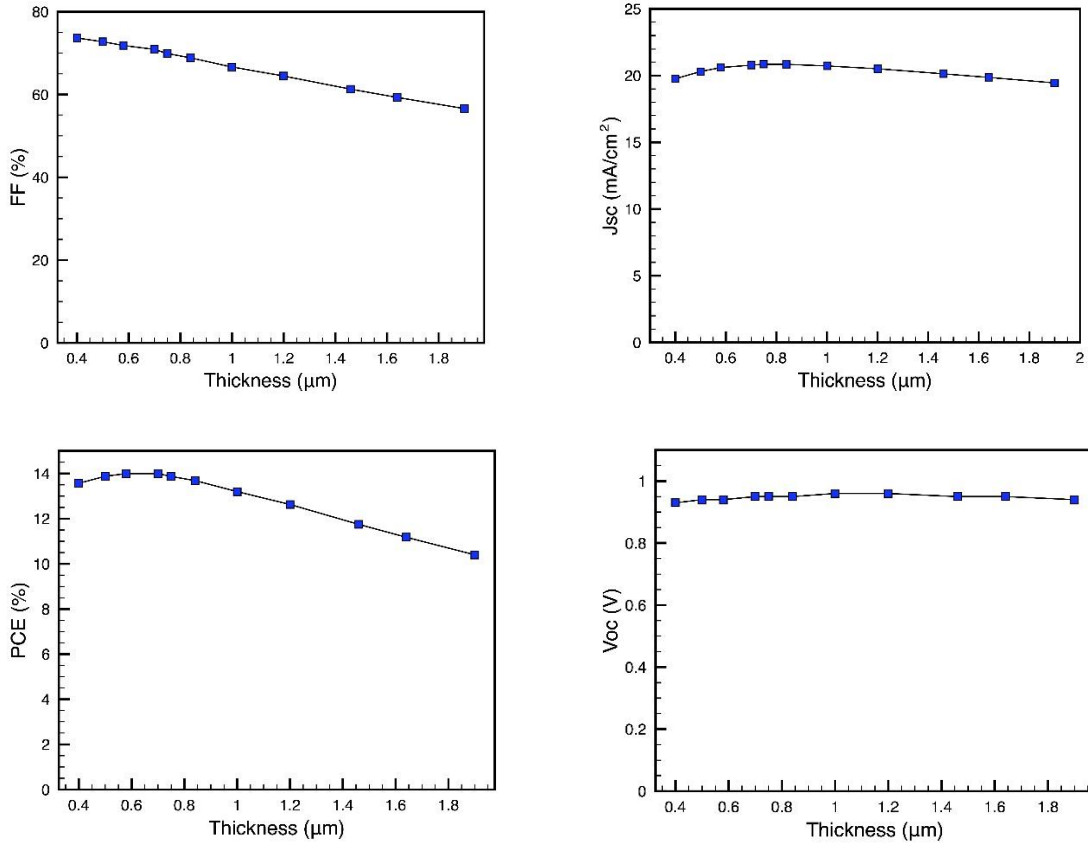
Figure 28. Effect of MAPbI3 thickness on solar cell performance

To investigate the MAPbI$_3$/HTL interface trap density effect on solar cell performance, we set the MAPbI$_3$/HTL interface defect density as variables (1×10^{11} to 1×10^{16} cm^{-3}), with other parameters constant (Table 2 and Table 3). Then, we did the simulation and obtained the solar cell performance parameters. Later, the active layer defect density and MAPbI$_3$/HTL interface defect density were controlled. The ETL/Perovskite interface defect density were variables. Figure 29 showed both the ETL/Perovskite and Perovskite/HTL interface defect density above 1×10^{13} cm^{-3} had not significantly affected the solar cell performance, with 1V open circuit voltage, 20.2 mA/cm^2 short circuit current, 72 % of fill factor, and 14.5 % power conversion

efficiency. However, when the ETL/Perovskite defect density was below 1×10^{13} cm^{-3}, both the

FF and short circuit density gained rapidly and reached 80% (the light enters from ETL) and

20.2 mA/cm^2, respectively (Chouhan et al. 2018).
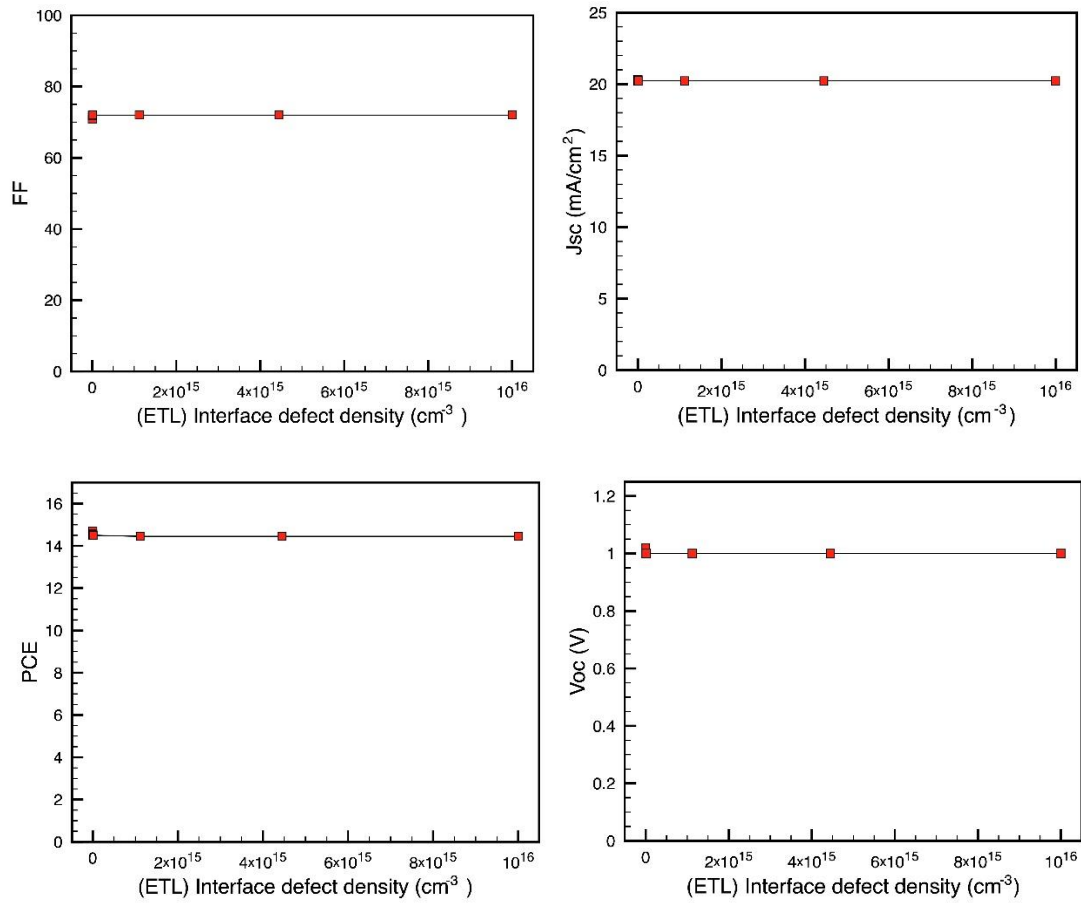
Figure 29. Effect of ETL/Perovskite interface defect density on solar cell performance
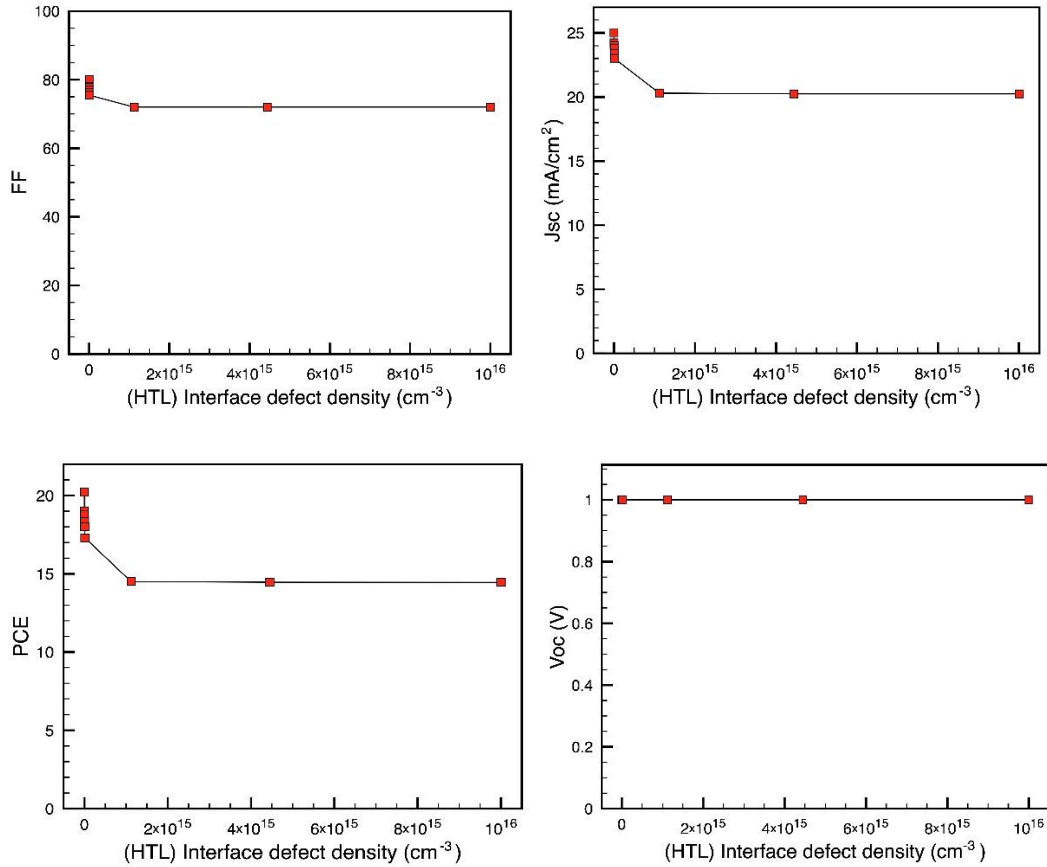
Figure 30. Effect of Perovskite/HTL interface defect density on solar cell performance

In contrast, the solar cell performance depended significantly on the perovskite layer. The active layer defect density above the threshold of 1×10^{14} cm^{-3} showed low performance devices. In addition, the thickness of the active layer had a rare effect on V_{oc} and J_{sc}. However, the thicker layer reduced the FF and had a threshold of around 0.7 µm on PCE. Furthermore, the interface defect density investigation showed the prone device performance, and both J_{sc} and V_{oc} were shown independent when the interface defect density was above 1×10^{13} cm^{-3}.

4.2.2 Concentrator simulation

We used 'COMSOL Multiphysics' to do the simulation. The simulation included the CPC, CPC trough and DPT (vertical absorber). Most of the simulation results included the acceptance angle and concentration efficiency of each concentrator.

Because the software cannot change the ray incident angle, we rotated the 3D model to obtain the efficiency at different angles. Below, we discuss the ray simulation results and assume that the source point is far away from the object. From this point, even the ray is not ideally parallel. However, compared to the real situation, the ray propagation can be seen as parallel if the concentrator is small enough and the distance between the light source and concentrator is long. Figure 31 depicts the light source used. The system efficiency was determined by counting the number of rays shooting on the absorber.
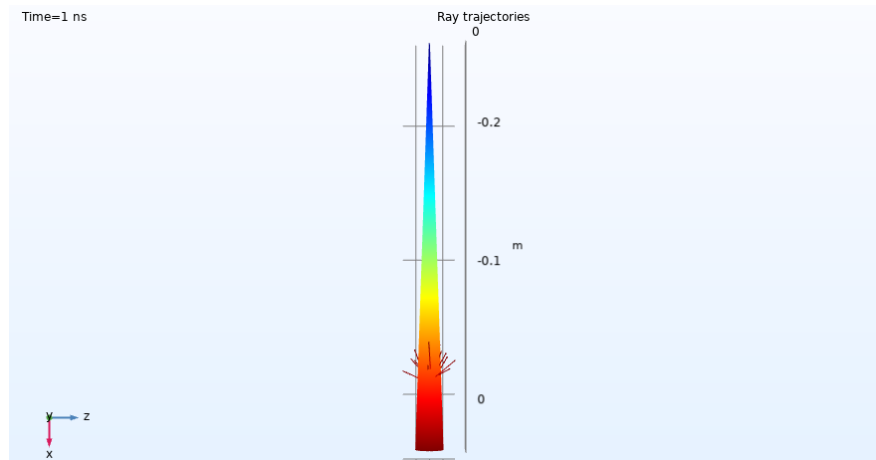
Figure 31. Asymptotically parallel rays

We simulated the CPC while rotating it from 0 degrees to 57 degrees. The efficiency remained over 80% before the CPC rotation angle is 20 degrees, and it drops exponentially after that.

0-degree	5-degree	10-degree
15-degree	20-degree	27-degree
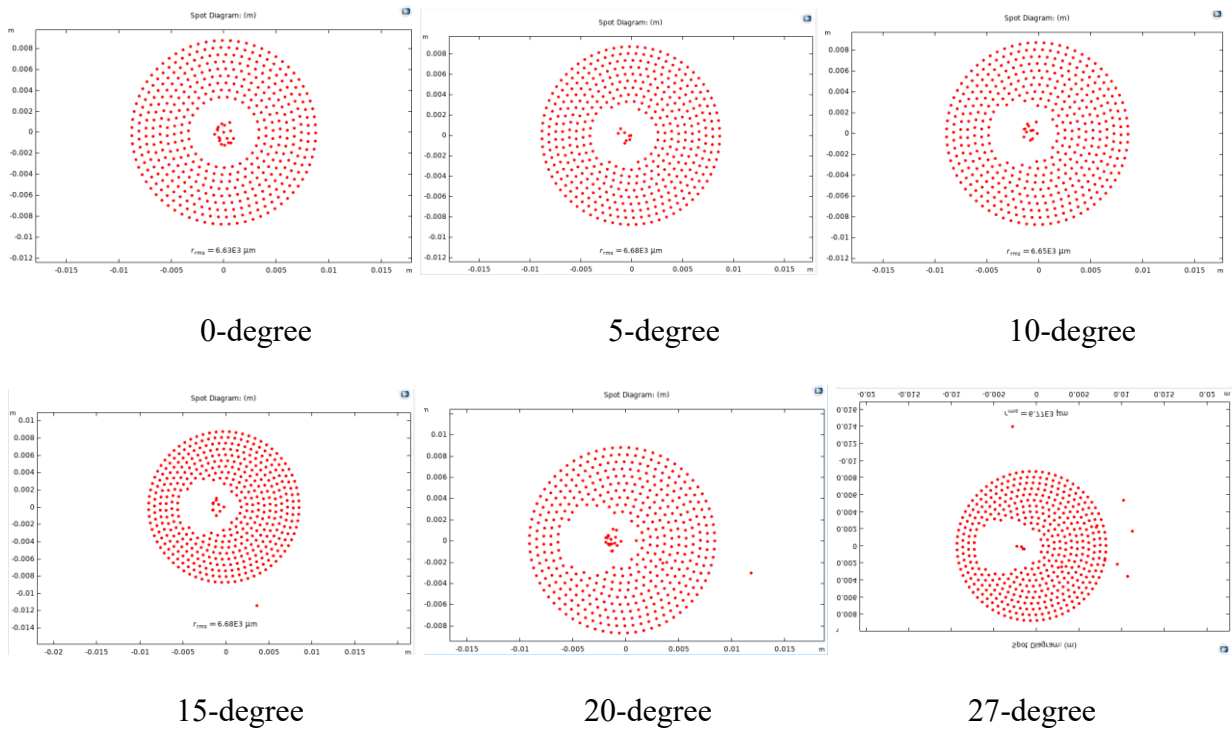
Figure 32. CPC absorber spots diagram

From the spots diagram, we can see that when the incident angle within the acceptance is a half angle, the efficiency remained over 90%. However, if the incident angle is 27 degrees, which is just a little greater than 26 degrees, the efficiency dropped to 20%.
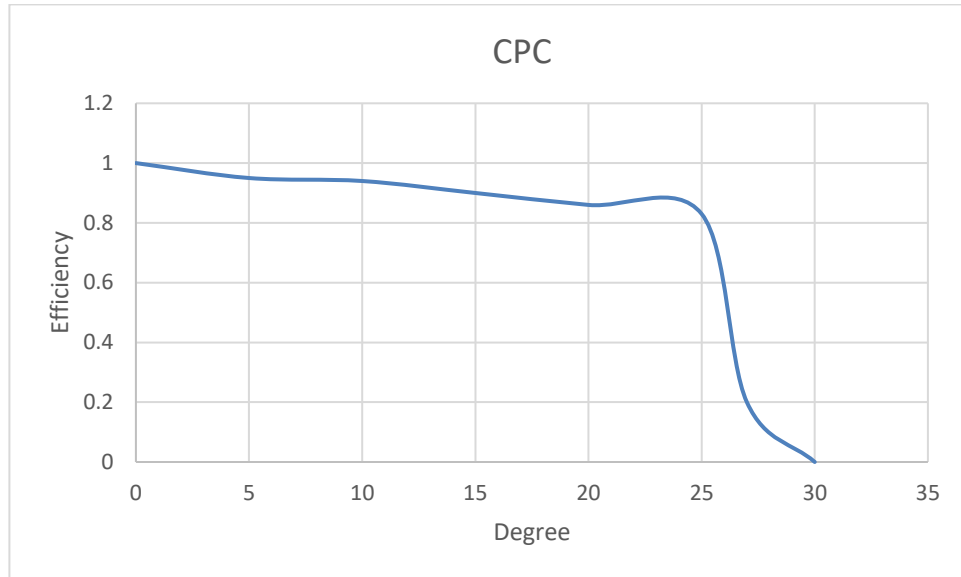
Figure 33. CPC efficiency

During the simulation, we found that when the light incident angle growth, a gap appeared between the absorber and the concentrated light, meaning that the light rays did not reach the absorber. The reason for that is shown in Figure 34. To prevent the issue happening in CPC, we built the vertical absorber to obtain a better acceptance angle and efficiency; the simulation process and results will be shown in the DPT part. Figure 34 below shows the 'gap'.

| 22-degree | 27-degree | 37-degree | 57-degree |
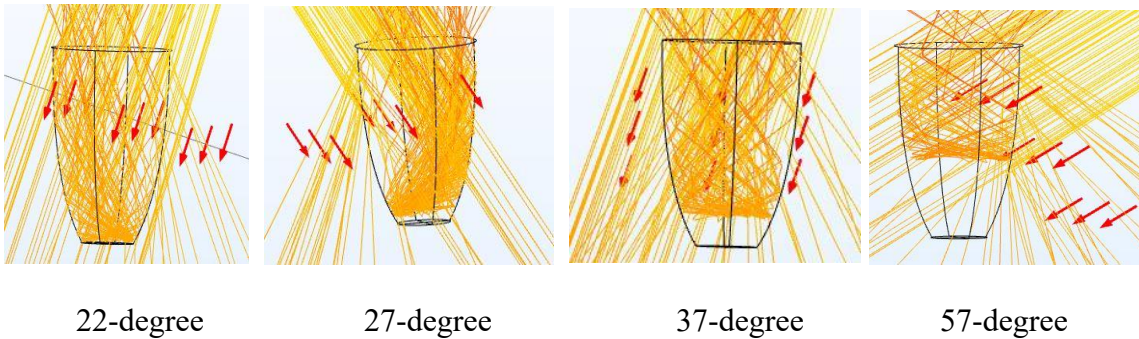
Figure 34. 'gap' between absorber and ended light

The CPC trough we designed included the height, length, theoretical acceptance angle and output diameter (absorber width). The setting of both side parabolic mirrors was 'mixed diffuse and specular reflection,' and the absorber (bottom) was 'freeze.'

We expected that, if the output diameter of concentrator was fixed, then the height and acceptance angle would have had an inverse relationship. For example, the CPC trough model in this simulation had the output diameter of 2.5 mm. If we accepted that the acceptance angle had 23 degrees, then, from the formula:

$$f = a'(1 + sin\theta_c)$$

$$h = \frac{f cos\theta_c}{sin^2\theta_c}$$

We can determine the height is 20.96 mm. If we choose the acceptance angle with 50 degrees, then the height is 4.84 mm. Figure 35 shows the two CPC trough 3D models with 23-degree and 50-degree acceptance angles.

(a)   (b)
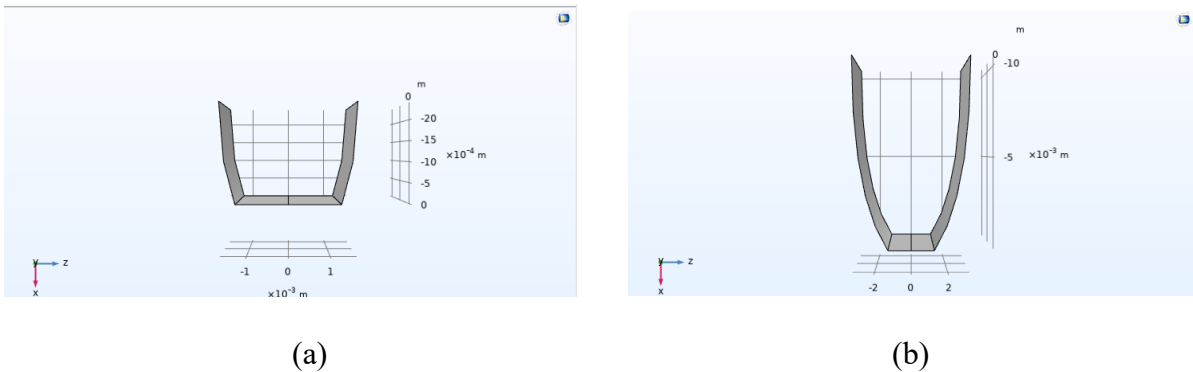
Figure 35. Acceptance angle versus CPC trough shape (a) 50-degree acceptance angle CPC trough and (b) 23-degree acceptance angle CPC trough

To determine the acceptance angle and concentration efficiency, we simulated the CPC trough

with rotations of 5 degrees, 10 degrees, 15 degrees, 20 degrees and 25 degrees, respectively.

Figure 36 below illustrates the acceptance angle versus varies incident angles.

0-degree	5-degree	10-degree
15-degree	20-degree	25-degree
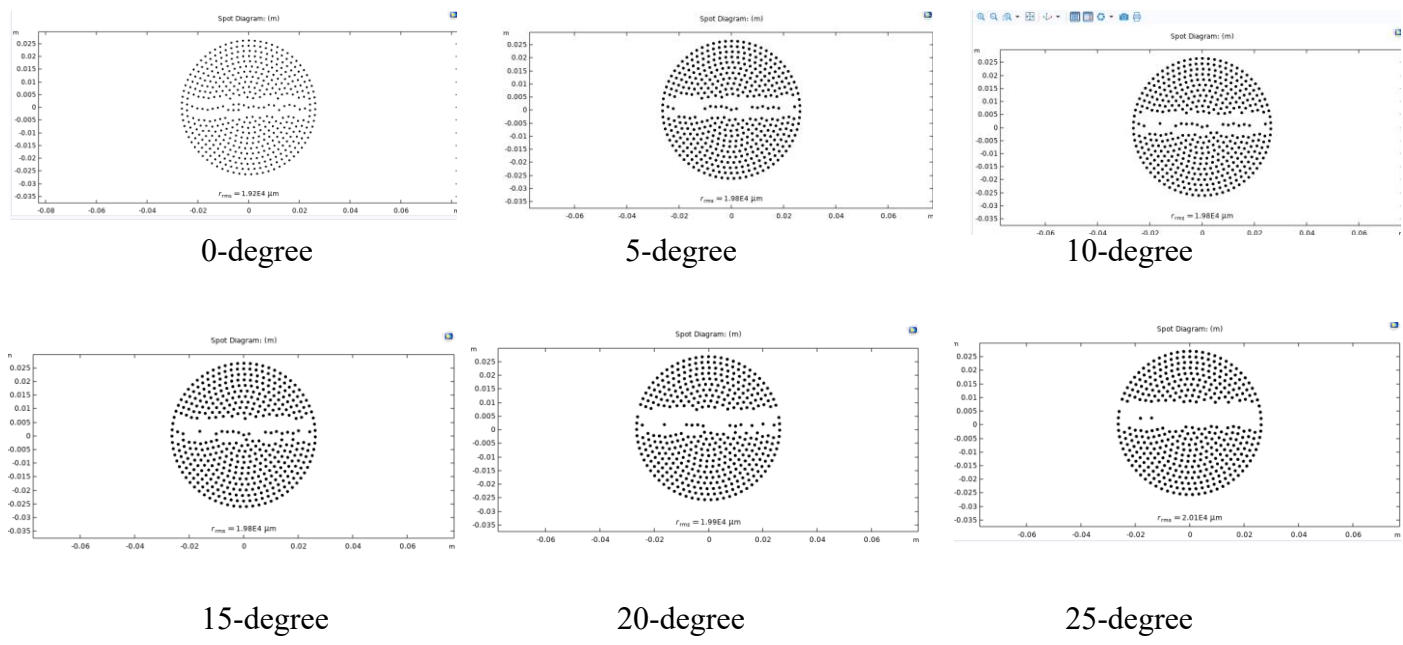
Figure 36. CPC trough absorber spot diagram

From the diagram, we can see the ray distribution at absorber. From 0 degrees to 20 degrees, the

ray is concentrated. When the concentrator rotation exceeds the acceptance angle, it cannot

concentrate the light. The diagram below shows the efficiency of the CPC trough concentration:
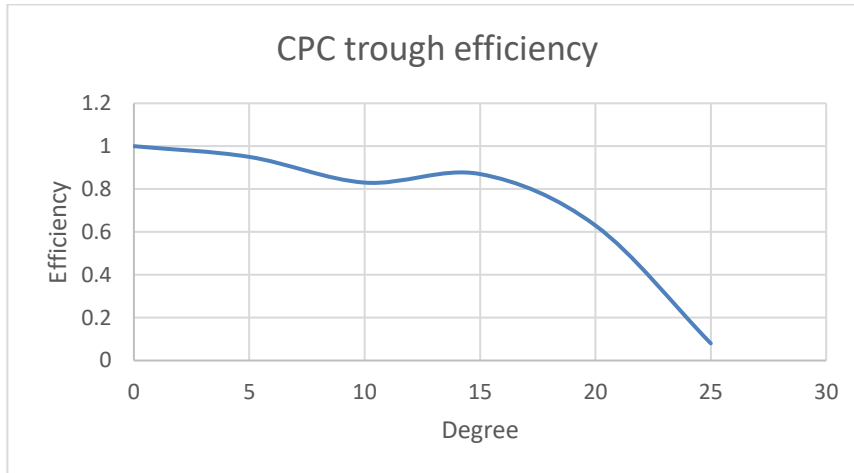
Figure 37. CPC trough efficiency

The efficiency remained above 80% before the 15-degree incident angle and it began to drop from 15 degrees to 20 degrees. When the incident angle was larger than 23 degrees, the efficiency decreased significantly.

The Double Parabolic Trough (DPT) concentrator is designed by each CPC trough. Because the DPT had a more complex shape, we constructed two CPC troughs and set part of the component as air, which may have affected the simulation results. The absorber of DPT was a vertical block that was located in the middle of two CPC troughs. The height of the absorber was flexible. In this simulation, we considered the absorber height to be 5 mm. The rest of the parts were mirrors which reflected all the incident light. The absorber spot diagrams are shown below:

0-degree | 5-degree | 10-degree

15- degree | 20-degree | 25-degree

30-degree | 40-degree | 50-degree

65-degree | 70-degree
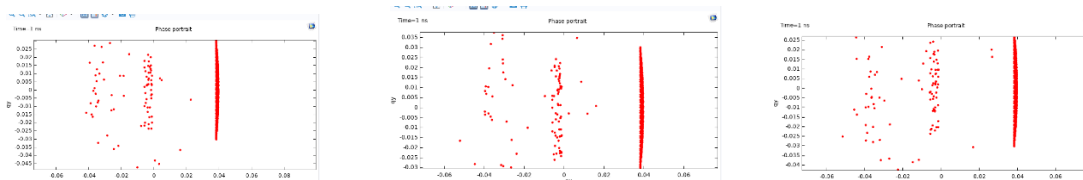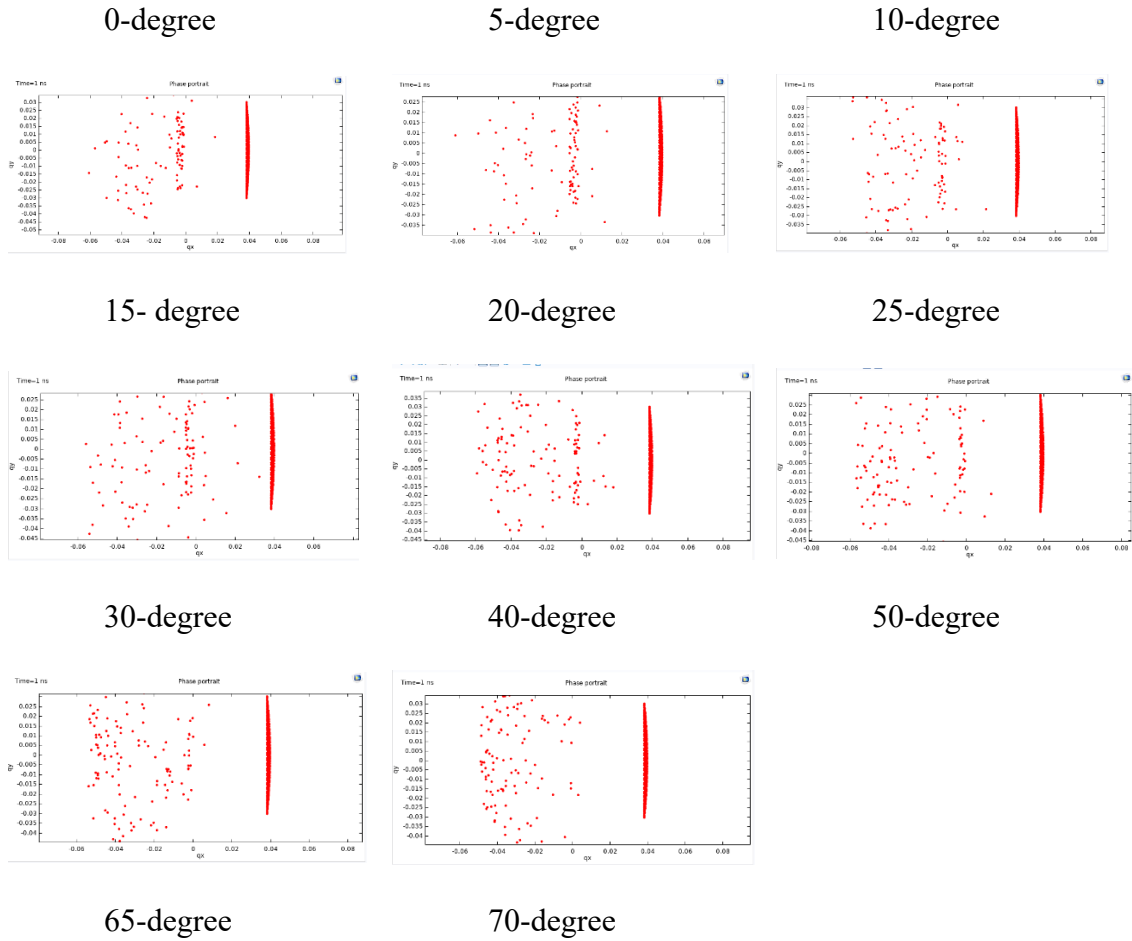
Figure 38. DPT vertical absorber spots diagram

The simulation shows the ray distribution of DPT with the vertical absorber. The spot diagram shows the y-z plane. The middle of the diagram shows the result that we are concerned with. The figure shown below is an example of the ray distribution.
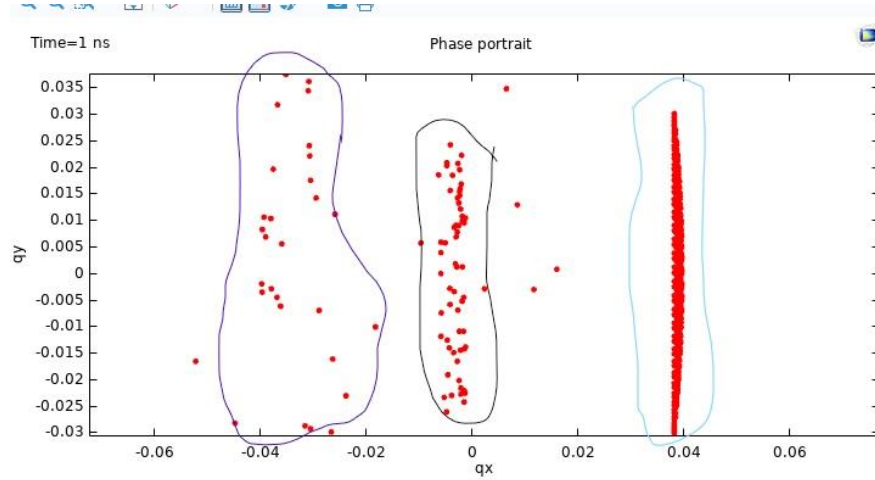
Figure 39. Ray distribution at 0-degree

At the far right, circled by light blue, is the ray ending area. The spots in middle, circled by black, shows ray distribution at vertical absorber. At left is the scattered light. From the spots diagram, we see that even at a 70-degree rotation angle, the DPT concentrator still could collect the light and that the efficiency compared to 0 degree was 19%. The efficiency remained above 90% until 20 degrees of concentrator rotate angle; it dropped slightly from 25 degrees to 50 degrees. At 65 degrees, the efficiency reached 48%. The diagram below indicates the overall DPT concentration efficiency.
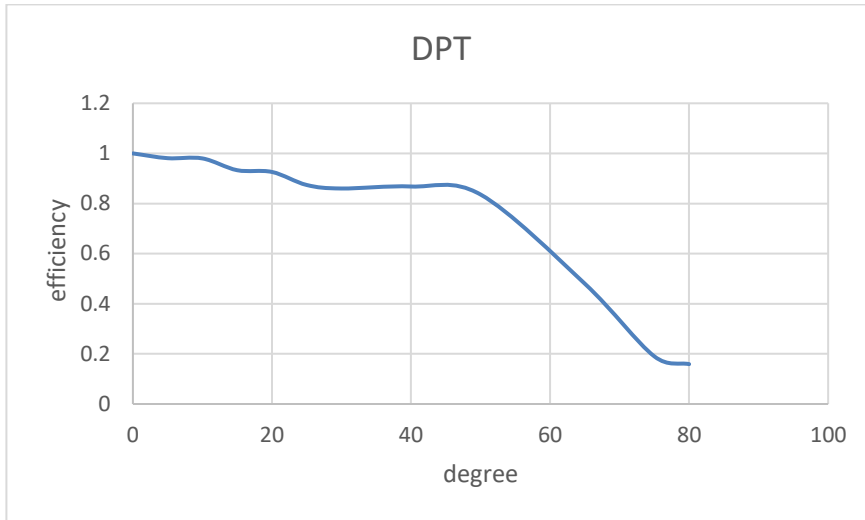
Figure 40. DPT concentration efficiency

CHAPTER 5   Conclusions

In this study, the perovskite films were prepared by the doctor blade coating technique using DMF-DMSO mixture solvent and high-concentration MA cation that has never been investigated before. The optoelectronic properties, surface roughness, and crystal size were changed significantly when the solvent ratio and MA cation concentration were changed. During the solar cell simulation, the effects of different morphologies, active layer thicknesses, defect densities and interface trap densities of the films were investigated. The results showed the PSC performance closely depended on perovskite layer defect density and thickness. In the solar concentrator simulation, we simulated the CPC, CPC trough, and DPT concentration efficiencies. As there has no relative reference support me to simulate the concentrator efficiency. I build the simulated nature sunlight and concentrator 3D module by using COMSOL-Multiphysics. The results show, the DPT, as a non-tracking light concentrator, showed the best performance with a wide range of acceptance angles and it kept high efficiency (over 80%) up to 50 degrees.

In recent years, perovskite materials were rapidly developed, but stability is still a problem since the perovskite materials degrade easily in high humidity environments. In addition, large-scale PSCs face an obvious decrease in the PCE due to the device nonuniformity and active area loss from interconnection (Wang et al. 2021). Therefore, popularizing the PSCs from laboratory-scale to photovoltaic market need further exploration and consideration. On the other hand, the potential threat of Pb leakage is an inevitable obstacle in the commercialization process (Wang et al. 2021). Thus, future studies, with stability of the perovskite material as its primary purpose. In addition, we only investigated the effect of MA cation on properties of perovskite samples.

The effect of BX (PbI$_2$) was not shown in this study and can be investigated in the future.

BIBLIOGRAPHY

1. Zhong, Yufei, et al. "Blade-Coated Hybrid Perovskite Solar Cells with Efficiency > 17%: An In Situ Investigation." ACS Energy Letters, vol. 3, no. 5, 2018, pp. 1078–1085.

2. Hsu, Hung-Chieh, et al. "Long-Term Stable Perovskite Solar Cells Prepared by Doctor Blade Coating Technology Using Bilayer Structure and Non-Toxic Solvent." Organic Electronics, vol. 101, 2022, p. 106400.

3. Johnsson, Mats, and Peter Lemmens. "Perovskites and Thin Films—Crystallography and Chemistry." Journal of Physics. Condensed Matter, vol. 20, no. 26, 2008, p. 264001.

4. Prasanna, Rohit, et al. "Band Gap Tuning via Lattice Contraction and Octahedral Tilting in Perovskite Materials for Photovoltaics." Journal of the American Chemical Society, vol. 139, no. 32, 2017, pp. 11117–11124.

5. Kita, Takashi, et al. Energy Conversion Efficiency of Solar Cells. Springer Singapore.

6. Mbilo, Mwende, et al. "Correlation between the Morphology and the Opto-Electronic and Electrical Properties of Organometallic Halide Perovskite ($CH_3NH_3MH_3$) Thin Films." Materials Research Express, vol. 6, no. 7, 2019, p. 76431.

7. Jung, Minsu, et al. "Perovskite Precursor Solution Chemistry: from Fundamentals to Photovoltaic Applications." Chemical Society Reviews, vol. 48, no. 7, 2019, pp. 211–238.

8. Tian, Shi, et al. "A Facile Green Solvent Engineering for up-Scaling Perovskite Solar Cell Modules." *Solar Energy*, vol. 183, 2019, pp. 386–391.

9. Liu, Runzhong, and Ke Xu. "Solvent Engineering for Perovskite Solar Cells: a Review." Micro & Nano Letters, vol. 15, no. 6, 2020, pp. 349–353.

10. Cai, Bing, et al. "Solvent Engineering of Spin-Coating Solutions for Planar-Structured High-Efficiency Perovskite Solar Cells." Chinese Journal of Catalysis, vol. 36, no. 8, 2015, pp. 1183–1190.

11. Marques, Adriano S, et al. "Low-Temperature Blade-Coated Perovskite Solar Cells." Industrial & Engineering Chemistry Research, vol. 60, no. 19, 2021, pp. 7145–7154.

12. Diau, Eric Wei-Guang, and Chen, Peter Chao-Yu. Perovskite Solar Cells : Principle, Materials, Devices. World Scientific, 2018.

13. BURSCHKA, Julian, et al. "Sequential Deposition as a Route to High-Performance Perovskite-Sensitized Solar Cells." Nature (London), vol. 499, no. 7458, 2013, pp. 316–319.

14. Chen, Sheng, et al. "Spatial Distribution of Lead Iodide and Local Passivation on Organo-Lead Halide Perovskite." *ACS Applied Materials & Interfaces*, vol. 9, no. 7, 2017, pp. 6072–6078.

15. Sirbu, Dumitru, et al. "Layered Perovskites in Solar Cells: Structure, Optoelectronic Properties, and Device Design." *Advanced Energy Materials*, vol. 11, no. 24, 2021, pp. 2003877-n/a.

16. Levy, Michael Y., and Christiana Honsberg. "Rapid and Precise Calculations of Energy and Particle Flux for Detailed-Balance Photovoltaic Applications." Solid-State Electronics, vol. 50, no. 7-8, Elsevier Ltd, 2006, pp. 1400–05, https://doi.org/10.1016/j.sse.2006.06.017.

17. C.B.Honsberg and S.G.Bowden, "Photovoltaics Education Website," *www.pveducation.org*, 2019.

18. Pandey Ashok, et al. "Microbial Poly-3-Hydroxybutyrate and Related Copolymers." Industrial Biorefineries and White Biotechnology, Elsevier, 2015, pp. 434-445.

19. Shukla, Ashutosh Kumar, and Siavash Iravani. "Metallic Nanoparticles: Green Synthesis and Spectroscopic Characterization." Environmental Chemistry Letters, vol. 15, no. 2, Springer International Publishing, 2017, pp. 223–31, https://doi.org/10.1007/s10311-017-0618-2.

20. Li, Bairu, et al. "Chlorobenzene Vapor Assistant Annealing Method for Fabricating High Quality Perovskite Films." Organic Electronics, vol. 34, Elsevier B.V, 2016, pp. 97–103, https://doi.org/10.1016/j.orgel.2016.04.024.

21. Zhang, Congyang, et al. "Critical Role of Metal Ions in Surface Engineering Toward Brightly Luminescent and Stable Cesium Lead Bromide Perovskite Quantum Dots." Nanoscale, vol. 11, no. 6, Royal Society of Chemistry, 2019, pp. 2602–07, https://doi.org/10.1039/c8nr09350d.

22. Guo, Yanru, et al. "Influence of the MACl Additive on Grain Boundaries, Trap-State Properties, and Charge Dynamics in Perovskite Solar Cells." Physical Chemistry Chemical Physics: PCCP, vol. 23, no. 1, Royal Society of Chemistry, 2021, pp. 6162–617, https://doi.org/10.1039/d0cp06575g.

23. S, Aseena, et al. "Optimization of Layer Thickness of ZnO Based Perovskite Solar Cells Using SCAPS 1D." *Materials Today: Proceedings*, vol. 43, Elsevier Ltd, 2021, pp. 3432–37, https://doi.org/10.1016/j.matpr.2020.09.077.

24. Hossain, Mohammad I., et al. "Copper Oxide as Inorganic Hole Transport Material for Lead Halide Perovskite Based Solar Cells." Solar Energy, vol. 120, Elsevier Ltd, 2015, pp. 370–80, https://doi.org/10.1016/j.solener.2015.07.040.

25. Xiao, Xufeng, et al. "Enhanced Perovskite Electronic Properties via A-Site Cation Engineering." Fundamental Research, vol. 1, no. 4, 2021, pp. 385–92, https://doi.org/10.1016/j.fmre.2021.06.002.

26. Wang, Feng, et al. "Defects Engineering for High-Performance Perovskite Solar Cells." Npj Flexible Electronics, vol. 2, no. 1, 2018, pp. 1–14, https://doi.org/10.1038/s41528-018-0035-z.

27. Chouhan, Arun Singh, et al. "Effect of Interface Defect Density on Performance of Perovskite Solar Cell: Correlation of Simulation and Experiment." *Materials Letters*, vol. 221, 2018, pp. 150–53, https://doi.org/10.1016/j.matlet.2018.03.095.

28. Alzahrani, Mussad, et al. "Advances and Limitations of Increasing Solar Irradiance for Concentrating Photovoltaics Thermal System." Renewable & Sustainable Energy Reviews, vol. 138, 2021, p. 110517–, https://doi.org/10.1016/j.rser.2020.110517.

29. Philipps, Simon P., and Andreas W. Bett. "III-V Multi-Junction Solar Cells and Concentrating Photovoltaic (CPV) Systems." Advanced Optical Technologies, vol. 3, no. 5, 2014, pp. 469–78, https://doi.org/10.1515/aot-2014-0051.

30. Wang, Hongqiao, et al. "Progress in Perovskite Solar Cells Towards Commercialization—A Review." Materials, vol. 14, no. 21, 2021, p. 6569–, https://doi.org/10.3390/ma14216569.

APPENDIX

Sample number	MAI (mg)	PbI$_2$ (mg)	DMF (mL)	DMSO (mL)
sample1	63.6	184.4	0	1
sample2	63.6	184.4	0.1	0.9
sample3	63.6	184.4	0.2	0.8
sample4	63.6	184.4	0.3	0.7

Appendix table 1. Chemical and solvent concentration of solvent study

Sample number	MAI (mg)	PbI$_2$ (mg)	DMF (mL)	DMSO (mL)
sample1	63.6	184.4	0.2	0.8
sample2	70	184.4	0.2	0.8
sample3	76.3	184.4	0.2	0.8
sample4	82.7	184.4	0.2	0.8

Appendix table 2. Chemical and solvent concentration of MAI investigation

Sample number	MAI (mg)	PbI$_2$ (mg)	MACl (mg)	DMF (mL)	DMSO (mL)
sample1	76.3	184.4	0	0.2	0.8
sample2	76.3	184.4	3.4	0.2	0.8
sample3	76.3	184.4	6.8	0.2	0.8
sample4	76.3	184.4	13.5	0.2	0.8

Appendix table 3. Chemical and solvent concentration of MACl investigation

ETL/MAPbI$_3$	V$_{oc}$(V)	J$_{sc}$(mA/cm^2)	FF (%)	PCE (%)
1×10^{11}	1.02	20.24	70.9	14.7
6.2×10^{11}	1	20.3	71.9	14.56
2.3×10^{12}	1	20.24	72	14.52
4.5×10^{12}	1	20.23	72	14.5
6.7×10^{12}	1	20.23	72	14.5
1×10^{13}	1	20.23	72	14.5
1.12×10^{15}	1	20.23	72	14.45
4.45×10^{15}	1	20.23	72	14.45
1×10^{16}	1	20.23	72	14.45

Appendix table 4. Effect of ETL/Perovskite interface defect density on solar cell performance

MAPbI$_3$/HTL	V$_{oc}$(V)	J$_{sc}$(mA/cm^2)	FF (%)	PCE (%)
1×10^{11}	1	25	80	20.2
6.2×10^{11}	1	24.2	78	19
2.3×10^{12}	1	24	77.8	18.8
4.5×10^{12}	1	23.8	77	18.35
6.7×10^{12}	1	23.4	76.3	18
1×10^{13}	1	23	75.47	17.3
1.12×10^{15}	1	20.3	72	14.5
4.45×10^{15}	1	20.24	72	14.46

| 1×10^{16} | 1 | 20.24 | 72 | 14.45 |

Thickness(μm)	J_{sc}(mA/cm^2)	V_{oc}(V)	FF (%)	PCE (%)
0.4	19.76	0.93	73.67	13.57
0.5	20.3	0.94	72.75	13.88
0.58	20.6	0.94	71.85	14
0.7	20.78	0.95	70.9	14
0.75	20.85	0.95	69.9	13.87
0.84	20.84	0.95	68.86	13.69
1	20.72	0.96	66.65	13.2
1.2	20.51	0.96	64.47	12.63
1.46	20.13	0.95	61.29	11.75
1.69	19.86	0.95	59.3	11.18
1.9	19.45	0.94	56.6	10.4

Solar simulator (Figure 1) in this experiment is used to determine the current-voltage (I-V) curve of PV devices. The solar simulator work as a single-lamp system with PV devices placed in designated area. The PV devices has 1 inch × 1 inch slides area and eight contact terminals as shown in Figure 2, and each terminal has 0.079 cm^2 active area.
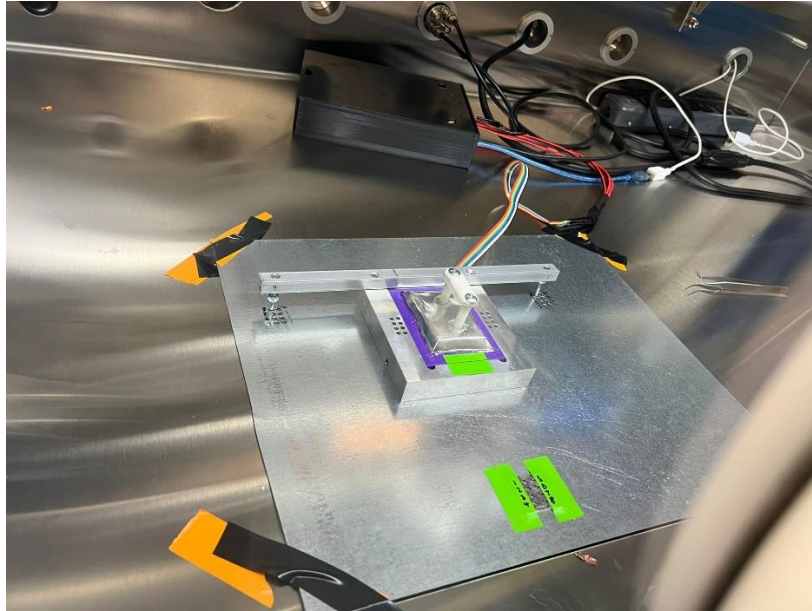
Appendix Figure 1. Solar simulator
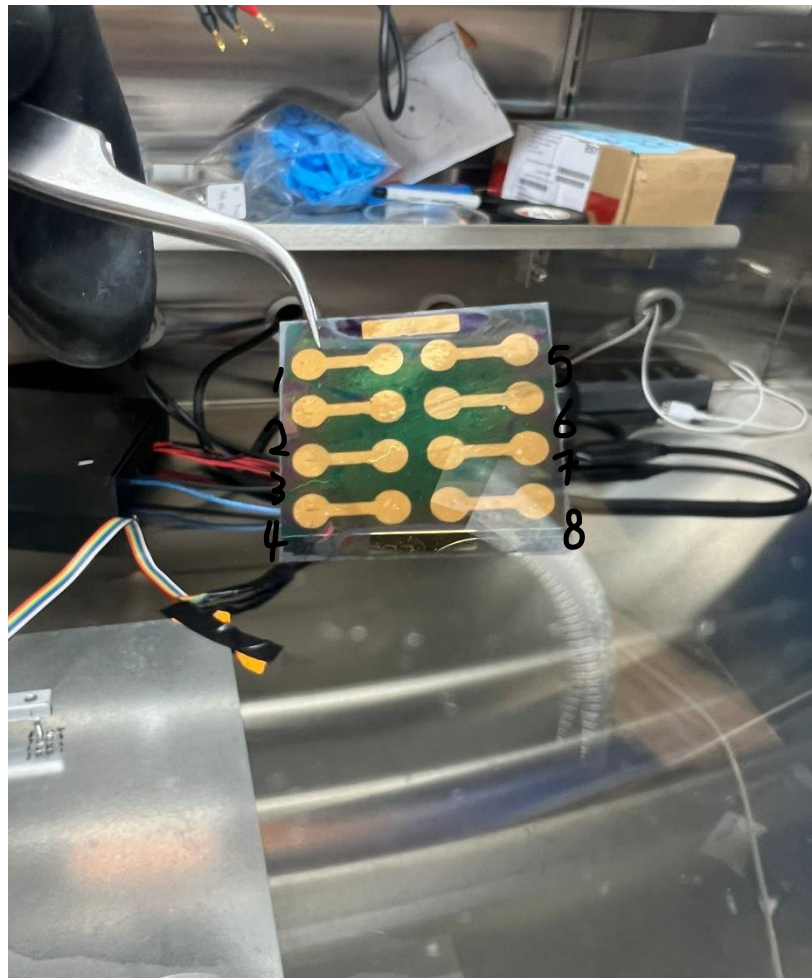
Appendix Figure 2. Perovskite solar cell devices